

African hydroclimate during the early Eocene from the DeepMIP simulations

Charles J. R. Williams^{1,2}, Daniel J. Lunt¹, Ulrich Salzmann³, Tammo Reichgelt⁴,
Gordon N. Inglis⁵, David R. Greenwood⁶, Wing-Le Chan⁷, Ayako Abe-Ouchi⁷, Yannick
Donnadieu⁸, David K. Hutchinson^{9,10}, Agatha M. de Boer⁹, Jean-Baptiste Ladant¹¹,
Polina A. Morozova¹², Igor Niezgodzki^{13,14}, Gregor Knorr¹⁴, Sebastian Steinig¹,
Zhongshi Zhang¹⁵, Jiang Zhu¹⁶, Matthew Huber¹⁷, Bette L. Otto-Bliesner¹⁶

¹School of Geographical Sciences, University of Bristol, UK

²NCAS / Department of Meteorology, University of Reading, UK

³Geography and Environmental Sciences, Northumbria University, UK

⁴Department of Geosciences, University of Connecticut, USA

⁵School of Ocean and Earth Science, University of Southampton, UK

⁶Department of Biology, Brandon University, Canada

⁷Atmosphere and Ocean Research Institute, The University of Tokyo, Japan

⁸Centre Européen de Recherche et d'Enseignement des Géosciences de l'Environnement,
France

⁹Department of Geological Sciences, Stockholm University, Sweden

¹⁰Climate Change Research Centre, University of New South Wales, Australia

¹¹Laboratoire des Sciences du Climat et de l'Environnement, France

¹²Institute of Geography, Russian Academy of Sciences, Russia

¹³Institute of Geological Sciences, Polish Academy of Sciences, Poland

¹⁴Alfred Wegener Institute for Polar and Marine Research, Germany

¹⁵Bjerknes Centre for Climate Research, University of Bergen, Norway

¹⁶Climate and Global Dynamics Laboratory, National Center for Atmospheric Research, USA

¹⁷Department of Earth, Atmospheric and Planetary Sciences, Purdue University, USA

Corresponding author address: School of Geographical Sciences, University Road, Bristol, BS8
1SS, UK

Email: c.j.r.williams@bristol.ac.uk

Short title: Early Eocene simulations of African hydroclimate

Keywords: Palaeoclimate, DeepMIP, Early Eocene, African precipitation

36 **KEY POINTS**

- 37 1) State-of-the-art climate models are used to study African hydroclimate during the early
38 Eocene (approximately 50 million years ago).
- 39 2) With increasing levels of CO₂, there are changes to African precipitation, due to dynamical
40 changes such as low level circulation.
- 41 3) A comparison between the models and newly-compiled climate estimates shows a marginally
42 better match at lower levels of CO₂.

43

44 **ABSTRACT**

45 The early Eocene (~56-48 million years ago) is characterised by high CO₂ estimates (1200-2500
46 ppmv) and elevated global temperatures (~10 to 16°C higher than modern). However, the response
47 of the hydrological cycle during the early Eocene is poorly constrained, especially in regions with
48 sparse data coverage (e.g. Africa). Here we present a study of African hydroclimate during the early
49 Eocene, as simulated by an ensemble of state-of-the-art climate models in the Deep-time Model
50 Intercomparison Project (DeepMIP). A comparison between the DeepMIP pre-industrial simulations
51 and modern observations suggests that model biases are model- and geographically dependent,
52 however these biases are reduced in the model ensemble mean. A comparison between the Eocene
53 simulations and the pre-industrial suggests that there is no obvious wetting or drying trend as the CO₂
54 increases. The results suggest that changes to the land sea mask (relative to modern) in the models
55 may be responsible for the simulated increases in precipitation to the north of Eocene Africa. There is
56 an increase in precipitation over equatorial and West Africa and associated drying over northern
57 Africa as CO₂ rises. There are also important dynamical changes, with evidence that anticyclonic
58 low-level circulation is replaced by increased south-westerly flow at high CO₂ levels. Lastly, a
59 model-data comparison using newly-compiled quantitative climate estimates from palaeobotanical
60 proxy data suggests a marginally better fit with the reconstructions at lower levels of CO₂.

61

62 **PLAIN LANGUAGE SUMMARY**

63 Approximately 50 million years ago, a period known as the early Eocene, atmospheric carbon dioxide
64 levels were significantly higher than today, and were more similar to what they could be in the future,
65 if efforts to reduce human greenhouse gas emissions are unsuccessful. However, rainfall changes
66 during this period are less well understood, especially over data-sparse regions such as Africa. Here, a
67 collection of state-of-the-art climate models are used to study African rainfall during this period,
68 comparing the simulations firstly to present-day African rainfall (to validate the models), secondly to
69 varying levels of atmospheric carbon dioxide, and lastly to newly-compiled reconstructions of early
70 Eocene rainfall (from plant fossils). The main findings are that although the models can reproduce
71 present-day rainfall over Africa, and compare reasonably well with the reconstructions, there is no
72 clear rainfall signal when atmospheric carbon dioxide is increased. Nevertheless, the combination of a

73 different continental configuration, vegetation, topography and atmospheric carbon dioxide leads to
74 changing rainfall patterns, connected to temperature and low level wind changes.
75

76 **1. INTRODUCTION**

77 One of the ways to better understand future anthropogenic-induced climate change is to simulate past
78 climates, using these as partial analogues for the future and allowing the testing of climate models to
79 simulate climates very different from today (Braconnot *et al.* 2011, Tierney *et al.* 2020). Simulating
80 past climates allows not only an interrogation of the mechanisms of past climate change (Haywood *et*
81 *al.* 2020, Lunt *et al.* 2021), but if a robust comparison with available proxy data can be produced, this
82 allows confidence in future climate change projections that are often based on models tuned to a
83 modern climate state (Harrison *et al.* 2014, Taylor *et al.* 2011, Williams *et al.* 2020, Williams *et al.*
84 2021, Zhu *et al.* 2020).

85

86 It has long been known that African precipitation, and in particular that over West Africa, is of vital
87 importance to the more than one billion people in sub-Saharan Africa who survive predominantly on
88 rain-fed agriculture and, concurrently, are highly vulnerable to extreme precipitation events causing
89 both flooding and drought (Williams and Kniveton 2011). However, a lack of weather and climate
90 data across much of the continent has resulted in a high level of uncertainty concerning both present
91 day and future climate trends (Salerno *et al.* 2019), and although it is expected that both average
92 temperature and precipitation will increase across Africa along with the rest of the world (IPCC
93 2021), regional variation is particularly high across Africa.

94

95 Due to their particular relevance to African precipitation, two Quaternary time periods have recently
96 been investigated by Williams *et al.* (2020) under the Palaeoclimate Modelling Intercomparison
97 Project (PMIP, Braconnot *et al.* 2007), now in its 4th phase and itself under the umbrella of the
98 Coupled Model Intercomparison Project, now in its 6th phase (CMIP6, Eyring *et al.* 2016). These
99 time periods are the mid-Holocene (6000 years ago, 6 ka) and Last Interglacial (127 ka). However,
100 excess warmth and enhancement of the Northern Hemisphere during these periods is caused primarily
101 by changes to the orbital configuration of Earth, rather than elevated greenhouse gases (Kageyama *et*
102 *al.* 2018). To investigate substantial greenhouse gas-induced warming, and its result on regional
103 hydroclimate such as across Africa, periods further back in time are needed, and two such candidates
104 in the context of PMIP are the mid-Pliocene (~3 million years ago, 3 Ma) and the early Eocene
105 (~56.05-47.8 Ma). However, with CO₂ levels ranging from 316-420 ppmv during the mid-Pliocene
106 (Martínez-Botí *et al.* 2015), this is more similar to modern levels rather than being a suitable analogue
107 for future projections by the end of the 21st century; using the previous RCP 8.5 scenario, this could be
108 over 1000 ppmv (IPCC 2013). The early Eocene, with CO₂ levels ranging between 1200-2500 ppmv
109 (Anagnostou *et al.* 2016, Anagnostou *et al.* 2020, Lunt *et al.* 2021), is comparable to the current future
110 projections, and in particular for the extended high-emissions/low-mitigation scenarios such as in the
111 year 2300 under SSP5-8.5 (Arias *et al.* 2021). As a result of this high CO₂, the early Eocene was a
112 period characterised by temperatures up to ~5°C higher than today in the tropics (e.g. Cramwinckel *et*

113 *al.* 2018, Gaskell *et al.* 2022, Inglis *et al.* 2020, Pearson and Wade 2007), and much greater polar
114 amplification with temperatures reaching ~20°C warmer than today at terrestrial high latitudes (e.g.
115 Huber and Caballero 2011, Naafs *et al.* 2018, van Dijk *et al.* 2020).

116

117 Despite being a partial analogue for future climate change, until the last few years climate model
118 simulations of high CO₂ periods such as the early Eocene have not been evaluated within a consistent
119 framework (Lunt *et al.* 2017); the closest to this was an informal model-data comparison, considering
120 four climate models, known as the Eocene Model Intercomparison Project (EoMIP), undertaken by
121 Lunt *et al.* (2012). This work focused on temperature-based metrics, however another study by
122 Carmichael *et al.* (2016) used the same EoMIP ensemble to look at the hydrological cycle and
123 hydroclimate changes in response to the elevated CO₂ levels in the early Eocene. The results focusing
124 specifically on Africa are discussed in more detail below but, globally, when compared to proxy data
125 it was found that the models generally underestimated precipitation over high latitudes, and those
126 models showing the most warming in these regions gave the best match to the data (Carmichael *et al.*
127 2016). Concerning the impact of elevated CO₂, it was found that all early Eocene simulations showed
128 a more intense hydrological cycle (relative to the pre-industrial era, hereafter PI), with enhanced
129 global precipitation and evaporation, and that this was generally directly related to the elevated
130 temperatures resulting from higher CO₂ (Carmichael *et al.* 2016). At any given level of CO₂, global
131 precipitation changes varied widely between models, and certain regions (such as tropical Africa,
132 discussed further below) were found to be sensitive to which model was assessed (Carmichael *et al.*
133 2016).

134

135 However, a disadvantage (albeit unavoidable) to EoMIP was that there was no consistent framework
136 to the models' experimental design; each used different boundary conditions (e.g. palaeogeography)
137 and different levels of CO₂ (Lunt *et al.* 2012). To resolve this problem, therefore, more recently the
138 Deep Time Model Intercomparison Project (DeepMIP) was envisaged and conducted, using CMIP3
139 and CMIP5 models as well as some of the most recent state-of-the-art CMIP6-class models (Lunt *et*
140 *al.* 2017). The large-scale features coming out of the simulations are discussed in Lunt *et al.* (2021),
141 with several conclusions being drawn. Firstly, boundary conditions other than CO₂, discussed in
142 Section 2.1, contributed between 3-5°C of the global mean early Eocene warming, relative to the PI
143 (Lunt *et al.* 2021). Secondly, the DeepMIP simulations showed less of a temperature spread than the
144 models in EoMIP, and an increase in climate sensitivity (Lunt *et al.* 2021). Lastly, when compared to
145 proxy SST data, most models reproduced the large-scale spatial patterns of the reconstructions but
146 still struggled at the regional scale, such as in the south-west Pacific (Lunt *et al.* 2021).

147

148 Similar to Lunt *et al.* (2012), Lunt *et al.* (2021) only focused on temperature and CO₂-based metrics.
149 The majority of recent studies looking at Eocene hydroclimate have focused on reconstructing

150 evidence for the Asian monsoon (e.g. Farnsworth *et al.* 2019, Ma *et al.* 2019, Licht *et al.* 2014, Quan
151 *et al.* 2012, Xie *et al.* 2019). There are very few studies, and in particular modelling studies, focusing
152 on Africa. The aforementioned study by Carmichael *et al.* (2016) using the EoMIP ensemble found
153 that tropical Africa was particularly sensitive to the model in question, and that the models varied in
154 skill (when reproducing precipitation, relative to observations) in regions of relatively low
155 precipitation such as over northern Africa's Sahel region. Moreover, although some models showed
156 similar PI precipitation over tropical Africa, under early Eocene conditions they were quite different
157 (Carmichael *et al.* 2016). It should be noted, however, that this study did not actually include any
158 early Eocene mean annual precipitation (MAP) reconstructions from Africa, only some Lutetian
159 samples (~41-47 Ma). More recently, Carmichael *et al.* (2018) ran several CO₂ simulations using just
160 the UK Met Office Hadley Centre model HadCM3L, finding an increase in both the size and
161 frequency of extreme precipitation events over equatorial and East Africa. Although MAP changes
162 were relatively small, extreme rainfall increased by up to 70% over parts of tropical Africa, with
163 summer precipitation events dominating the regime over southern Africa (Carmichael *et al.* 2018).
164 Another example of Eocene African work is that of Liu *et al.* (2019), who looked at the Asian,
165 African and Australian monsoons across five different time periods and found that precipitation from
166 the African monsoon existed as early as the mid-Paleocene. Keery *et al.* (2018) found the variability
167 of Asian and African precipitation during the Eocene was predominantly accounted for by orbital
168 configuration changes such as the precession and obliquity; in DeepMIP, however, these were kept at
169 PI values and so, here, the impact on African precipitation will only be down to the CO₂ or the other
170 boundary condition changes.

171

172 In this paper four main questions are addressed:

- 173 1) How well do the DeepMIP models' PI simulations reproduce modern observations of African
174 precipitation?
- 175 2) What is the impact of CO₂ and other early Eocene boundary conditions on African
176 precipitation in the DeepMIP models' early Eocene simulations?
- 177 3) What are the physical mechanisms behind this precipitation response?
- 178 4) How do the DeepMIP models' early Eocene simulations compare with proxy data of African
179 precipitation?

180

181 Section 2 of this paper briefly describes the experimental design followed by the DeepMIP models,
182 gives a brief introduction to the models themselves, and describes the observational and proxy data
183 used for comparative purposes. Section 3 presents the results, addressing each of the above questions.
184 Section 4 summarises and concludes.

185

186 **2. EXPERIMENT DESIGN, MODELS, AND PROXY DATA**

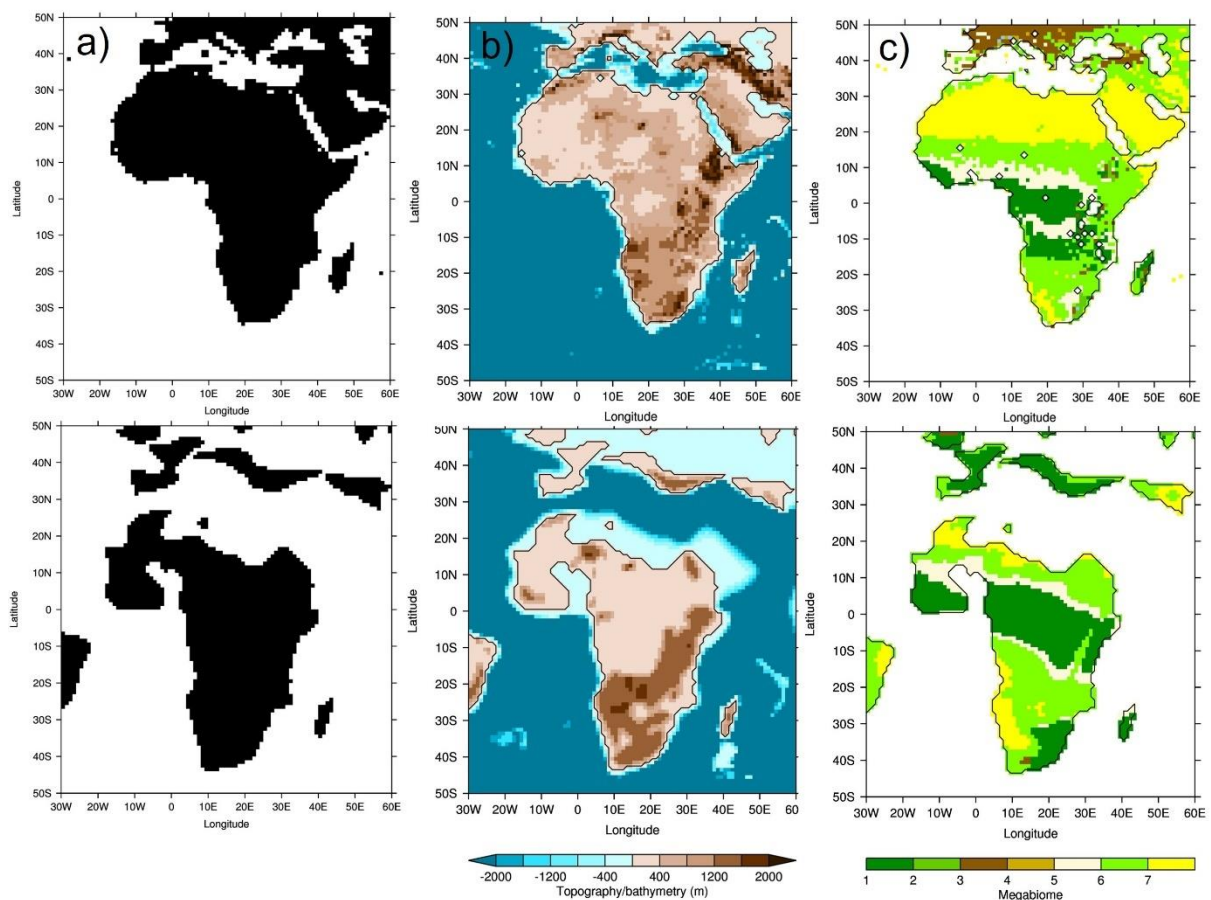
187 **2.1. Experiment design**

188 The full experimental design, which all DeepMIP modelling groups were required to follow as closely
 189 as possible, is detailed extensively in Lunt *et al.* (2017) and so will only be briefly outlined here. In
 190 addition to the various CO₂ experiments, all modelling groups were required to carry out a PI
 191 simulation for comparison purposes, which was to be as close as possible to the CMIP6 standard
 192 *piControl* simulation (Eyring *et al.* 2016).

193

194 For the early Eocene simulations, a number of boundary conditions needed to be changed, the key
 195 ones for the African region of which are shown in Figure 1.

196



197

198 Figure 1 – Main boundary conditions changed in DeepMIP simulations, where top row = PI and bottom row =
 199 early Eocene: a) Land sea mask; b) Topography/bathymetry; c) Vegetation, expressed as megabiomes according
 200 to Harrison and Prentice (2003) (where 1 = Tropical, 2 = Warm-temperate, 3 = Temperate, 4 = Boreal, 5 =
 201 Savanna, 6 = Grassland and 7 = Desert). The PI topography/bathymetry is taken from ETOPO5, re-gridded to
 202 1°x1° resolution, whereas the other fields are from Herold *et al.* (2014)

203

204 Firstly, the land sea mask (LSM) was based on the palaeogeographic heights (discussed further
 205 below), with possible manual manipulation required in some models to maintain the various gateways
 206 (Lunt *et al.* 2017). The new LSM produced a geographically smaller Africa relative to the PI, with

207 much of the present-day landmass north of 20°N being ocean in the early Eocene due to the increased
208 sea level (Figure 1a). Secondly, the palaeogeography (including topography and bathymetry) was
209 based on the digital reconstruction of the early Eocene from Herold *et al.* (2014), with the topography
210 (and sub-grid scale topography) being applied as an absolute value rather than as an anomaly (Lunt *et*
211 *al.* 2017). Over Africa, the most pronounced changes were over southern and eastern Africa, with
212 generally larger areas of raised topography in the early Eocene, relative to the PI (Figure 1b). This
213 can be seen more clearly in the Supplementary Material, where the differences in topography are
214 shown; there is clearly a large increase in elevation over western Africa where there is land in the
215 early Eocene but ocean in the PI, but apart from this (where the landmasses coincide) the largest
216 changes are over southern and eastern Africa (Figure S1). Thirdly, concerning the land surface,
217 vegetation and river run-off routing was also based on the dataset of Herold *et al.* (2014), using an
218 appropriate lookup table to convert the vegetation megabiomes into whatever format was required by
219 the model (Lunt *et al.* 2017). The early Eocene vegetation was created by running the dynamic
220 vegetation model BIOME4 (Kaplan *et al.* 2003), with the resulting 27 biomes being consolidated into
221 10 megabiomes following the procedure of Harrison and Prentice (2003); please see Table 3 in
222 Harrison and Prentice (2003) for a distinction between these megabiomes. BIOME4 itself was forced
223 by Eocene topography, bathymetry and CO₂ coming out of an early Eocene simulation from the
224 CESM climate model. Concerning how well the simulated vegetation compares with reconstructions,
225 Herold *et al.* (2014) state that it compares well with vegetation inferred from Palaeocene and Eocene
226 palynoflora (Utescher and Mosbrugger 2007, Morley 2007), and is consistent with geological
227 indicators of climate (Crowley 2012). Although Herold *et al.* (2014) highlight a dry bias in vegetation
228 over South America, there is no specific mention of Africa, primarily because there is currently little
229 or no palaeobotanical data for Africa, meaning validation was not possible. Although it is beyond the
230 scope of this study to modify the vegetation boundary conditions, previous work has suggested a high
231 sensitivity to vegetation, showing for example dramatically increased global annual mean
232 temperatures when interactive vegetation is used, compared to fixed vegetation (Loftson *et al.* 2014).
233

234 When compared to the PI, over Africa the new vegetation resulted in: i) a loss of the desert regions
235 over the present-day Sahara, primarily because this is ocean in the early Eocene; ii) a latitudinal
236 expansion (relative to the PI) of tropical rainforest across central Africa; and iii) an addition of a large
237 area of tropical rainforest over southern Africa, which is savanna or grassland in the PI (Figure 1c).
238 However, some features remained similar in the early Eocene relative to the PI, such as the region of
239 tropical rainforest across central Africa being bordered by savannah to the north and south, and the
240 Namib Desert (Figure 1c). The impact on precipitation of these three boundary condition changes is
241 discussed below. Soil parameters, including soil dust fields, were given a globally constant value, and
242 (given the lack of palaeodata) no lakes were prescribed unless dynamically predicted (Lunt *et al.*
243 2017). Concerning greenhouse gas concentrations, the CO₂ experiments were divided into a set of

244 standard experiments (which all modelling groups should ideally have conducted) and a set of
 245 sensitivity experiments (which were optional). All of these were expressed as multiples of the PI
 246 simulation, typically with a CO₂ of 280 ppmv, and were as follows: 3x and 6x the PI for the standard
 247 experiments, and 1x, 1.5x, 2x, 4x and 9x the PI for the sensitivity experiments (Lunt *et al.* 2017). See
 248 Table 1 for which modelling groups conducted which experiments. All other greenhouse gases were
 249 kept as PI, the justification for which is given in Lunt *et al.* (2017). Concerning aerosols, given the
 250 rapid development of representation of aerosols in models the experimental design was flexible here
 251 and allowed modelling groups to either leave these as PI, treat aerosols interactively (if possible),
 252 prescribe aerosols from Herold *et al.* (2014), or a combination of the above (Lunt *et al.* 2017). The
 253 solar constant and astronomical parameters were kept identical to the PI, the justification for which is
 254 again given in Lunt *et al.* (2017).

255

Modelling group responsible	Model	Atmospheric resolution (lon x lat)	CO₂ experiments undertaken	Run length (years)	References
University of Michigan, US	CESM1.2_CAM5	2.5° x 1.89°	1x, 3x, 6x, 9x	2000	Hurrell <i>et al.</i> (2013)
Alfred Wegener Institute, Germany / Polish Academy of Sciences, Poland	COSMOS-landveg_r2413	3.75° x 3.71°	1x, 3x, 4x	9500	Jungclaus <i>et al.</i> (2006)
Stockholm University, Sweden	GFDL_CM2.1	3.75° x 3.05°	1x, 2x, 3x, 4x, 6x	6000	Delworth <i>et al.</i> (2006)
University of Bristol, UK	HadCM3B_M2.1aN	3.75° x 2.5°	1x, 2x, 3x	7800	Valdes <i>et al.</i> (2017)
University of Bristol, UK	HadCM3BL_M2.1aN	3.75° x 2.5°	1x, 2x, 3x	7800	Valdes <i>et al.</i> (2017)
National Academy of Sciences, Russia	INM-CM4-8	2° x 1.5°	6x	1050	Volodin <i>et al.</i> (2018)
Laboratoire des Sciences du Climat et de l'Environnement, France	IPSLCM5A2	3.75° x 1.89°	1.5x, 3x	4000	Sepulchre <i>et al.</i> (2020)
University of Tokyo, Japan	MIROC4m	2.8125° x 2.79°	1x, 2x, 3x	5000	Chan <i>et al.</i> (2011)
University of Bergen, Norway	NorESM1_F	2.5° x 1.89°	2x, 4x	2100	Guo <i>et al.</i> (2019)

256

257 Table 1 - Models taking part in DeepMIP, including relevant details and references

258

259 Lastly, the experimental design provided some advice on practical matters such as simulation length
260 and output format. The simulations varied in length (see Table 1) but were all at least 1000 years in
261 length, with the climatologies, comprising the results discussed here, being calculated over the final
262 100 years. At that point, all simulations should have had a global mean top-of-the-atmosphere (TOA)
263 net radiation balance of less than 0.3 W m^{-2} (or a similar balance to that of the PI) and an SST trend of
264 less than $0.1^\circ\text{C century}^{-1}$ (Lunt *et al.* 2017). All of the output, details of which are given in Lunt *et al.*
265 (2017), were uploaded to a centralised DeepMIP database.

266

267 **2.2. Models**

268 Extensive details on each model, and how the experimental design was implemented in their
269 simulations, are given in Lunt *et al.* (2021) and references therein and will therefore only briefly be
270 discussed here; those aspects likely to affect precipitation (e.g. convection and land-surface schemes)
271 will be focused upon here. In total, nine models were included in DeepMIP, although it should be
272 noted that two of these are different configurations of the same model. See Table 1 for a list of the
273 models, along with their atmospheric spatial resolutions and appropriate references (particularly
274 relating to the atmospheric component of the models and elements relating to hydroclimate, where
275 available). In detail, these are as follows.

276

- 277 • CESM1.2_CAM5: The Community Earth System Model version 1.2 (CESM1.2) is comprised
278 of the Community Atmosphere Model version 5.3 (CAM5), the Community Land Model
279 version 4.0, the Community Ice Code version 4.0 and the Parallel Ocean Program version 2
280 (Hurrell *et al.* 2013). CAM5 uses the finite-volume dynamical core and physical
281 parameterizations of deep convection (Zhang and McFarlane 1995), shallow convection and
282 moist turbulence (Park and Bretherton 2009), and cloud microphysics (Morrison and
283 Gettelman 2008). This version contains new physical parameterisations in the atmosphere,
284 such as the cloud microphysics, which is critical for the simulation of the large-scale climate
285 features of the early Eocene (Liu *et al.* 2017)
- 286 • COSMOS-landveg_r2413: For an atmospheric general circulation model, ECHAM5 (the
287 European Centre Hamburg Model) is used (Roeckner *et al.* 2003), and this is coupled to the
288 Max-Planck-Institute for Meteorology Ocean Model (MPIOM) (Marsland *et al.* 2003); the
289 coupled model is described by Jungclaus *et al.* (2006). COSMOS-landveg_r2413 simulates
290 cumulus convection using a mass flux scheme. The orography is represented in spectral
291 domain by surface geopotential (see Stepanek and Lohmann 2012 for more details regarding
292 model description). The land surface conditions for each biome are based on Hagemann
293 (2002); additionally, parameters with a seasonal cycle (i.e. leaf area index and vegetation
294 ratio) in the latitude belt of $\sim 20^\circ\text{S}$ - 20°N were smoothed and an annual average for each biome
295 was prescribed.

- 296 • GFDL_CM2.1: This uses the Geophysical Fluid Dynamics Laboratory (GFDL) CM2.1 model
 297 (Delworth *et al.* 2006), with modifications as described in Hutchinson *et al.* (2018), and
 298 comprising the Atmosphere Model 2, Land Model 2 and the Sea Ice Simulator 1, coupled to
 299 the ocean component from the modular ocean model version 5.1 (MOM5.1). The atmosphere
 300 uses a finite-volume discretisation, and a 3° latitude x 3.75° longitude resolution with 24
 301 vertical levels, following the configuration of CM2Mc (Galbraith *et al.* 2011). Convection is
 302 parameterised by the relaxed Arakawa-Schubert scheme of Moorthi and Suarez (1992), with a
 303 lower-bound on entrainment as specified in Tokioka *et al.* (1988). Cloud microphysics are
 304 parameterised using the scheme of Rotstajn (1997), while cloud macrophysics use the
 305 parameterisation of Tiedtke (1993). Full details of the convection and cloud
 306 parameterisations are given in Delworth *et al.* (2006). Of possible relevance to the simulation
 307 of precipitation, the topography is smoothed using a three-point mean filter to allow a
 308 smoother interaction with the wind field (Lunt *et al.* 2021).
- 309 • HadCM3B_M2.1aN: This Hadley Centre Climate Model (HadCM3) version is documented
 310 extensively in Valdes *et al.* (2017). In particular, the model uses a single ‘bulk’ cloud model
 311 to parameterise dry as well as shallow and deep moist convection (Grant 1998). The cloud
 312 scheme uses a statistical parametrization via a probability density function over the grid-box
 313 total water content (Bushell 1998). Six short-wave and eight long-wave radiation bands are
 314 represented by the scheme of Edwards and Slingo (1996). Static fields for the nine surface
 315 types of the MOSES2.1 land surface scheme (Cox *et al.* 1999) are derived from the ten
 316 megabiomes of the DeepMIP vegetation boundary conditions (Herold *et al.* 2014) via a
 317 lookup table. The atmosphere uses a Cartesian grid with a horizontal resolution of 3.75 x 2.5°
 318 (longitude x latitude) and 19 hybrid vertical levels.
- 319 • HadCM3BL_M2.1aN: The only difference between this version of HadCM3 and the one
 320 described above is the horizontal resolution of the ocean component (Cox 1984), at 1.25° x
 321 1.25° for HadCM3B_M2.1aN and 3.75° x 2.5° for HadCM3BL_M2.1aN, and associated
 322 diffusion parameters (Valdes *et al.* 2017). Both versions use 20 unequally spaced vertical
 323 levels in the ocean ranging between 10 and 616 m.
- 324 • INM-CM4-8: This version of the Institute of Numerical Mathematics (INM) model is
 325 described in Volodin *et al.* (2018), but the parameterisations of physical processes are the
 326 same as in the previous version, INM-CM5, and described more detail in Volodin *et al.*
 327 (2017). Parameterization of condensation and cloud formation follows Tiedtke (1993), and
 328 cloud water is a prognostic variable. Parameterization of cloud fraction follows Smagorinsky
 329 (1963); cloud fraction is a diagnostic variable, independent of the calculation of condensation,
 330 and depended on the relative humidity. Deep and shallow convection is parameterized by
 331 Bets (1986). The surface, soil and vegetation scheme follow Volodin and Lykossov (1998),

332 with the evolution of the equations for temperature, soil water and soil ice being solved at 23
333 levels from the surface to 10 meters depth (Volodin *et al.* 2018). The fractional area of 13
334 types of potential vegetation is specified, and actual vegetation as well as LAI is calculated
335 according to the soil water content in the root zone and soil temperature (Volodin *et al.* 2018).

- 336 • IPSLCM5A2: The IPSL-CM5A2 Earth system model from the Institut Pierre Simon Laplace
337 (IPSL) is documented by Sepulchre *et al.* (2020), and is based on the previous generation
338 IPSL Earth system model (IPSLCM5A, Dufresne *et al.* 2013) but with new revisions such as
339 a re-tuning of global temperature. It comprises the LMDZ5 (Laboratoire de Météorologie
340 Dynamique Zoom) atmosphere model, the Organising Carbon and Hydrology In Dynamic
341 Ecosystems (ORCHIDEE) land surface and vegetation model and the Nucleus for European
342 Modeling of the Ocean (NEMOv3.6) ocean model, which includes the LIM2 sea ice model
343 and the Pelagic Interactions Scheme for Carbon and Ecosystem Studies (PISCESv2)
344 biogeochemical model (Lunt *et al.* 2021). LMDZ5 runs at a horizontal resolution of $1.9^\circ \times$
345 2.5° (latitude \times longitude) with 39 hybrid sigma-pressure levels. The LMDZ5 radiation
346 scheme is inherited from the European Center for Medium-Range Weather Forecasts
347 (Fouquart and Bonnel 1980, Morcrette *et al.* 1986), and the dynamical effects of the subgrid-
348 scale orography are parameterized according to Lott (1999). Turbulent transport in the
349 planetary boundary layer is treated as a vertical eddy diffusion (Laval *et al.* 1981), with
350 counter-gradient correction and dry convective adjustment, and the surface boundary layer is
351 treated according to Louis (1979). Cloud cover and cloud water content are computed using a
352 statistical scheme (Bony and Emanuel 2001). For deep convection, the LMDZ5A version
353 uses the “episodic mixing and buoyancy sorting” scheme originally developed by Emanuel
354 (1991).
- 355 • MIROC4m: This version of the Model for Interdisciplinary Research on Climate (MIROC) is
356 documented by K-1 model developers (2004) and summarized in Chan *et al.* (2011). In the
357 atmosphere model, cumulus parameterization is based on Arakawa and Schubert (1974), with
358 some simplifications and the cloud base mass flux is treated as a prognostic variable.
359 Cumulus convection is suppressed when the cloud-mean ambient relative humidity is less
360 than the critical value of 0.8. The land surface model (Minimal Advanced Treatments of
361 Surface Interaction and Runoff, MATSIRO) is documented by Takata *et al.* (2003), where
362 prognostic variables include canopy temperature, canopy water content, snow amount, soil
363 moisture content and frozen soil moisture content. Fixed vegetation types are specified over
364 ice-sheet-free. The ocean component is version 3.4 of the CCSR (Center for Climate System
365 Research) Ocean Component Model (COCO), documented in Hasumi (2000).
- 366 • NorESM1_F: This version of the Norwegian Earth System Model (NorESM) is described in
367 detail in Guo *et al.* (2019) and Li *et al.* (2020), and differs from the previous version

368 (NorESM1-M) in that while it has the same atmosphere-land grid, the ocean and sea ice
369 components use a tripolar grid (rather than the bipolar grid in NorESM1-M), resulting in a
370 more realistic Atlantic Meridional Overturning Circulation (Lunt *et al.* 2021). NorESM1_F
371 couples the Miami Isopycnic Coordinate Ocean Model (MICOM) and the spectral
372 Community Atmosphere Model (CAM4) (Eaton 2010, Neale *et al.* 2008, Neale *et al.* 2013).
373 CAM4 includes the Zhang and McFarlane (1995) deep convection scheme, the Hack (1994)
374 shallow convection scheme, the nonlocal boundary layer scheme of Holtslag and Boville
375 (1993) and the representation of cloud microphysics and macrophysics by Rasch and
376 Kristjánsson (1998) and Zhang *et al.* (2003). Instead of using the undiluted convective
377 available potential energy (CAPE) in the original deep convection scheme, the diluted CAPE
378 through an explicit representation of entrainment has been used to close the cumulus
379 parameterization (Neale *et al.* 2008). The convective momentum transport has also been
380 included in the parameterization of deep convection (Richter and Rasch 2008). Additionally,
381 NorESM1_F adopts energy updates and energy conservation. Compared to NorESM1-M,
382 NorESM1_F has several important improvements on how precipitation is simulated, such as
383 improvements in seasonality, a reduced wet bias and mitigation of the common double
384 intertropical convergence zone (ITCZ) problem (Li *et al.* 2020).

385

386 **2.3. Observational and proxy data**

387 Here the observational and proxy data are described; firstly there is a description of the modern,
388 satellite-derived data used to assess and evaluate the PI simulations, and secondly there is a
389 description of the early Eocene proxy data used to evaluate the Eocene simulations.

390

391 ***2.3.1. Satellite-derived rainfall estimates from the modern period***

392 Even in the 21st century, there is a severe lack of in-situ rain gauge data over Africa; South Africa is
393 probably the best populated in terms of rainfall measurements, but in other countries such as Angola
394 or Namibia rain gauge data are sparse or non-existent (e.g. Williams *et al.* 2007, Williams *et al.* 2008,
395 Williams *et al.* 2010). The CenTrends precipitation dataset (Funk *et al.* 2015) contains measurements
396 going back to 1900, but only for a small number of countries in East Africa. Likewise, although the
397 Global Historical Climate Network (GHCN) database (Durre *et al.* 2008, Durre *et al.* 2010, Menne *et*
398 *al.* 2012) does contain temperature measurements going back to 1861, precipitation measurements do
399 not begin until the 1950s and are again relatively sparse in Africa. Therefore, a possible solution to
400 the problem of data unavailability is to use satellite-derived rainfall estimates (SREs), which offer
401 near-uniform coverage at relatively high spatial resolution from the 1980s onwards.

402

403 Several datasets of SREs currently exist, but here the Tropical Applications of Meteorology using
404 SATellite data and ground-based observations (TAMSAT) is used. TAMSAT (version 3.1) provides

405 daily, 10-daily, monthly and seasonal precipitation estimates over Africa at 4 km resolution, and
406 extends from 1983 to the present-day. The data are publicly available; please see Open Research
407 section, and Maidment *et al.* (2014), Maidment *et al.* (2017) and Tarnavsky *et al.* (2014) for details.
408 Here, TAMSAT is used as a comparative tool for evaluating the PI simulations of the DeepMIP
409 models. A caveat here is that the models are showing precipitation simulated under PI boundary
410 conditions, whereas TAMSAT is showing precipitation from the late 20th and early 21st century
411 (referred to here as modern) and will therefore contain an anthropogenic signal; this, however, is
412 unavoidable given the lack of PI precipitation observations. It is expected that the biases between
413 comparing the models to PI precipitation versus comparing them to modern precipitation will be less
414 than the biases between the models themselves (i.e. the inter-model spread), and indeed much less
415 than the uncertainty associated with the Eocene reconstructions.

416

417 **2.3.2. Palaeobotanical Eocene precipitation estimates**

418 The distribution and physiognomy of land plants are sensitive to precipitation (Wright *et al.* 2017).
419 Therefore, the taxonomic affinity and the morphology of leaf fossils can be used to generate palaeo-
420 precipitation estimates (e.g. Utescher *et al.* 2014, Wilf *et al.* 1998). For this study, previously
421 established Paleocene-Eocene (~41-56 Ma) palaeobotanical records from Africa were compiled (see
422 Supplementary Material for age ranges for individual sites, Table S1). The distribution of the nearest
423 living relatives (NLR) of these taxa was then analyzed using the bioclimatic analysis approach to find
424 the highest probability precipitation range in which all taxa could co-occur (e.g. West *et al.* 2020,
425 Willard *et al.* 2019).

426

427 Geodetic coordinates of occurrences were obtained for the NLR of each plant group from the Global
428 Biodiversity Information Facility (GBIF) (see Supplementary Material, Table S2). These occurrence
429 datasets were then filtered for uncertain, exotic and superfluous occurrences, as well as subjected to a
430 random resampling to avoid regional overrepresentation of densely sampled areas. A climatic
431 envelope for each plant group (see Table S2) was then generated by extracting precipitation data
432 (mean annual precipitation (MAP), wettest month (WMP), driest month (DMP), warmest and coldest
433 quarter precipitation (WQP and CQP, respectively) and the precipitation seasonality coefficient (PS))
434 using the DISMO package in R (Hijmans *et al.* 2005). A probability density function was then
435 generated for each co-occurring plant group by testing the likelihood of the plant group occurring at
436 100,000 unique extant combination of MAP, WMP, DMP, PS, WQP and CQP. As shown in
437 Equation 1, the product of probabilities (f) was calculated for each plant group (t) at each climatic
438 combination (x), using the means (μ) and standard deviations (σ) of their modern-day bioclimatic
439 envelope, for each climatic variable (c).

440

441
$$f(t_n) = \prod_{i=1}^6 \frac{1}{\sqrt{2\sigma_c^2} \times \pi} e^{x_c - \mu_c / 2\sigma_c^2}$$

442 Equation 1

443

444 A combined likelihood for all plant groups in the assemblage combined can then be calculated with
 445 the product of all likelihoods (n), shown in Equation 2.

446

447
$$f(z) = \prod_{i=1}^n t_n$$

448 Equation 2

449

450 The combination of MAP, WMP, DMP, PS, WQP and CQP with the highest likelihood is the value
 451 reported here as most representative for the assemblage, and the highest and lowest values of the
 452 metrics with $f(z) \geq 5\%$ of the maximum $f(z)$ is represented as the uncertainty (using the 95%
 453 confidence interval).

454

455 Eleven plant assemblages from South Africa, Tanzania, South Sudan, Cameroon, Côte d'Ivoire,
 456 Ghana and Nigeria were analyzed with the bioclimatic analysis NLR method (Adeonipekun *et al.*
 457 2012, Atta-Peters and Salami 2004, Cantrill *et al.* 2013, Chiaghanam *et al.* 2017, de Villiers 1997,
 458 Eisawi and Schrank 2008, Goha *et al.* 2016, Okeke and Umeji 2016, Salami 1984, Salard-Chebouldaef
 459 1979, Uzodimma 2013); see Table S1 for age ranges of individual sites.

460

461 The NLR generated precipitation values were supplemented with an additional value based on leaf
 462 area analysis (LAA) derived data by Jacobs and Herendeen (2004) and Kaiser *et al.* (2006), also from
 463 Tanzania (from the Lutetian). In locations where the final results are in the same geographical
 464 location, the reconstructions were averaged. The final results of this analysis are shown in Table 2,
 465 with Eocene MAP expressed as ranges and modern MAP taken from TAMSAT. It should be noted
 466 that, for the results other than the model-data comparison, precipitation during June-August (JJA) is
 467 focused upon, rather than using MAP. Previous work has suggested that for much of the continent,
 468 over 80% of the annual total of precipitation is accounted for by a given region's wet season and, over
 469 West Africa (the wet season of which is JJA), this increases to 95% or higher (Liebmann *et al.* 2012).
 470 Given that the primary driver of this wet season is the seasonal progression of the ITCZ, it is likely
 471 that this relationship will hold during the early Eocene. It was therefore deemed appropriate to focus
 472 on this season for the majority of the analysis (i.e. Sections 3.1, 3.2 and 3.3), only using MAP for the
 473 model-data comparison (Section 3.4), for which seasonal proxy data are not available.

474

Site name	Latitude (°N)	Longitude (°E)	MAP (mm year ⁻¹)	
			Early Eocene	Modern
Koningsnaas, South Africa	-30.2	17.3	1318-1738	101
Shagamu, Nigeria	6.7	3.7	1148-2089	1762
Melut Basin, South Sudan	10	33	1175-1905	757
Kwakwa, Cameroon	4.5	9.1	1175-1905	2524
Mwadui, Tanzania	-3.9	33.5	813-1738	754
Tano, Ghana	4.7	-3	1514-2344	-
Nanka, Nigeria	6.12	7	1380-2291	1683
Abidjan margin, Côte d'Ivoire	5	-4.1	1660-1950	-
Okigwe, Nigeria	5.82	7.34	1175-1862	2311
Bende - Umuahia, Nigeria	5.47	7.45	1514-2291	2311
Araromi, Nigeria	7.7	3.5	1072-1738	1179
Mahenge, Tanzania	-4.79	34.26	720-800	707
Mahenge, Tanzania	-4.79	34.26	630-690	707
Mahenge, Tanzania	-4.79	34.26	737-815	707
Mahenge, Tanzania	-4.79	34.26	644-708	707
Mahenge, Tanzania	-4.79	34.26	710-790	707
Mahenge, Tanzania	-4.79	34.26	610-680	707
Mahenge, Tanzania	-4.79	34.26	610-680	707
Mahenge, Tanzania	-4.79	34.26	740-820	707

475

476 Table 2 - Locations and mean annual precipitation (MAP) from early Eocene palaeobotanical records from
477 Africa, and modern values. Early Eocene ranges of MAP are expressed as the 95% confidence interval for all
478 locations except Mahenge, where ranges are expressed as +/- 1 standard deviation. Modern values of MAP
479 taken from TAMSAT; missing values indicate ocean regions, as TAMSAT MAP is land only

480

481 3. RESULTS

482 Here the results of different comparisons are described: i) a model validation exercise, where the
483 models' PI simulations are compared to modern observations (Section 3.1); ii) a simulation

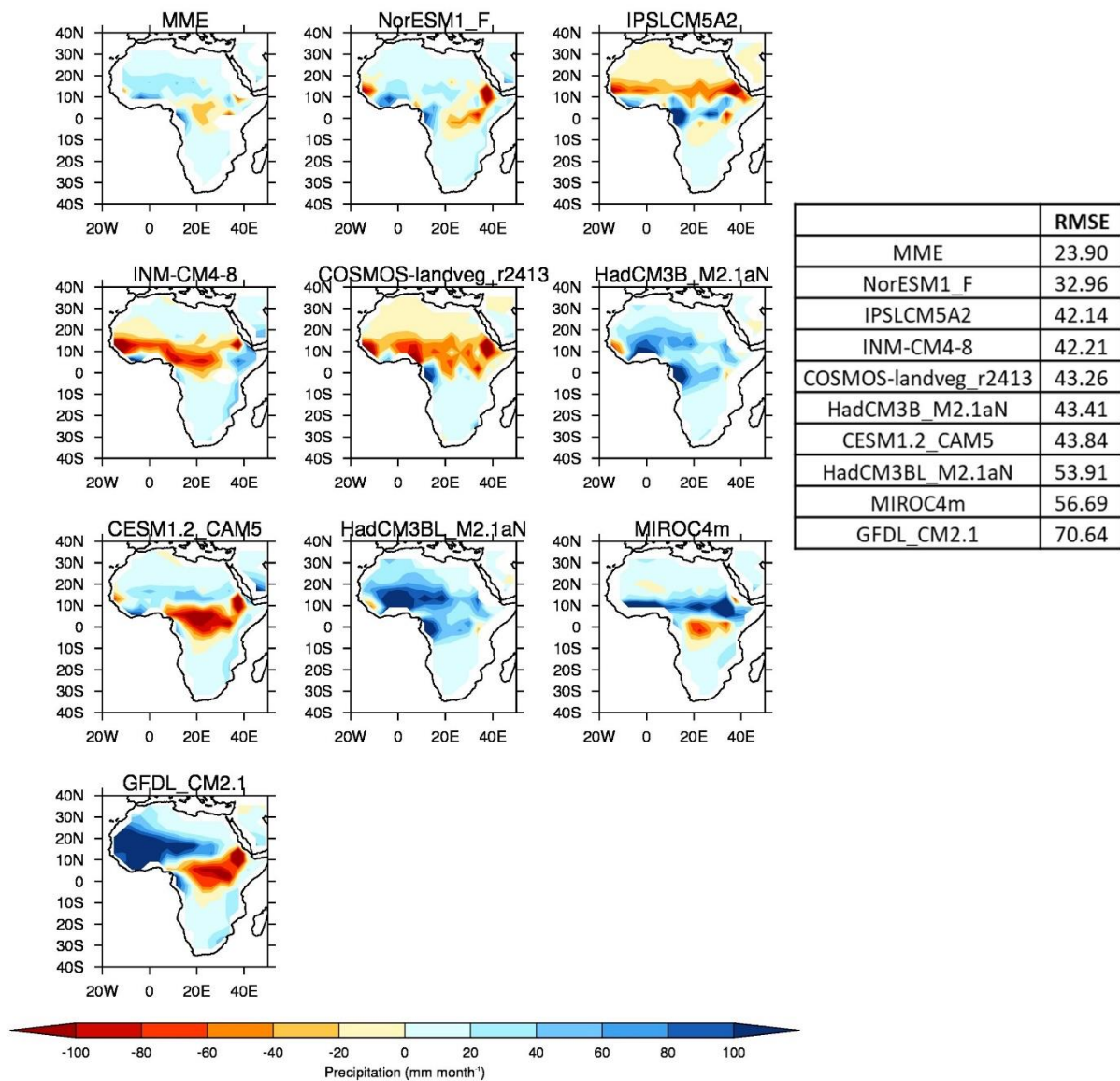
484 comparison, where precipitation from the models' early Eocene simulations, at varying levels of CO₂,
485 is compared (Section 3.2); iii) a simulation comparison, where the physical mechanisms behind the
486 precipitation response are investigated (Section 3.3); and iv) a model-data comparison, where
487 precipitation from the models' early Eocene simulations is compared to available proxy data (Section
488 3.4).

489

490 **3.1. DeepMIP models' preindustrial simulations versus modern observations**

491 Here the focus is on mean precipitation differences between the various DeepMIP PI simulations
492 (including the multi-model ensemble mean, MME) and precipitation observations from TAMSAT
493 (see Section 2.3.1). Here, the MME is calculated for a given variable as the simple mean across all
494 available models. Precipitation anomalies (PI simulations - TAMSAT) during JJA are shown in
495 Figure 2, where the models have been ordered according to the root mean square error (RMSE),
496 relative to TAMSAT. Two observations are noteworthy. Firstly, the MME is showing by far the
497 closest agreement to TAMSAT, with a much lower RMSE (by ~10 mm month⁻¹ less than even the
498 next lowest individual model), highlighting the importance of using the MME to counterbalance
499 individual models' biases (whether they be under or overestimating). The MME will therefore
500 subsequently be used when discussing the various Eocene simulations. Secondly, there appears to be
501 a divide between: a) models such as IPSLCM5A2, INM-CM4-8 and COSMOS-landveg_r2413 that
502 are underestimating African precipitation (i.e. are showing drier conditions across West Africa at
503 ~10°N), which have relatively low RMS error compared with TAMSAT; and b) models such as
504 HadCM3BL_M2.1aN, MIROC4m and GFDL_CM2.1 that are overestimating African precipitation,
505 which have relatively high RMS error compared with TAMSAT. For example, the model with the
506 least agreement (GFDL_CM2.1, RMSE = 70.6 mm month⁻¹) is overestimating precipitation over West
507 Africa by more than 100 mm month⁻¹.

508

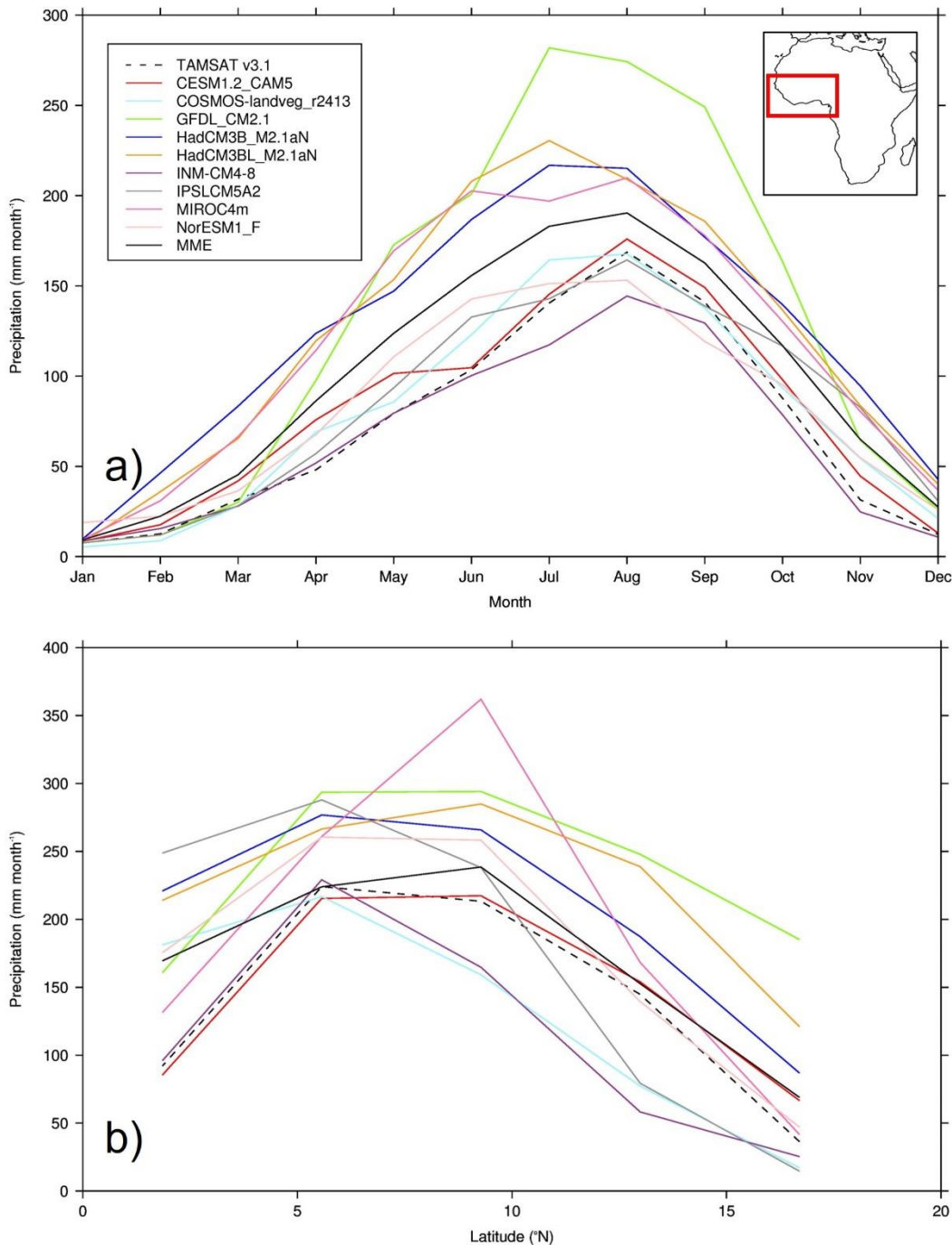


509

510 Figure 2 - JJA precipitation climatology differences (PI simulations - TAMSAT), re-gridded to lowest common
 511 spatial resolution (that of COSMOS-landveg_r2413) and ordered according to Root Mean Squared Error
 512 (RMSE, in mm month⁻¹, see insert). RMSE calculated over 20°W-50°E, 40°N-40°S, land points only
 513

514 Concerning the seasonal and latitudinal distribution of African precipitation, Figure 3 shows the
 515 annual cycle of West African (defined here as land points only encompassing 20°W-15°E, 0-20°N)
 516 precipitation and the zonal mean of JJA West African precipitation (Figure 3a and b, respectively).
 517 Outside of JJA, the majority of models are overestimating precipitation throughout the year (Figure
 518 3a), with the model closest to TAMSAT (in terms of the seasonal cycle i.e. precipitation timings)
 519 being CESM1.2_CAM5, although even this model overestimates precipitation during the first half of
 520 the year. When averaged over this region, only one model (INM-CM4-8) underestimates
 521 precipitation throughout the year, but is nevertheless closer to TAMSAT than those which
 522 overestimate, in agreement with that discussed above and shown in Figure 2. One model

523 (GFDL_CM2.1) greatly overestimates precipitation especially during JJA, and others (such as INM-
524 CM4-8) underestimate precipitation during JJA and therefore do not correctly reproduce the strong
525 seasonality (i.e. the precipitation curve is flatter); for example, the difference between the wettest and
526 driest month in this model is 136 mm month⁻¹, whereas it is 161 mm month⁻¹ in TAMSAT and 181
527 mm month⁻¹ in the MME (Figure 3a). The MME also overestimates precipitation throughout the year
528 but is nevertheless closer to TAMSAT in terms of seasonality than many of the wetter models (Figure
529 3a). Latitudinally, most models are showing a much wider (in terms of latitudinal extent) rain belt
530 relative to TAMSAT, with GFDL_CM2.1 and the HadCM3 family in particular not reproducing the
531 observed rapid drop-off in precipitation either near the Equator or north of 15°N (Figure 3b). In part
532 due to some drier models approaching the Equator (such as CESM1.2_CAM5 and INM-CM4-8), the
533 MME is showing a similar latitudinal extent of precipitation compared to TAMSAT, and while it is
534 still too wet at low latitudes it does correctly drop off north of 15°N (Figure 3b).
535



536

537 Figure 3 - Precipitation climatology from TAMSAT and PI simulations, averaged over West Africa (20°W-
 538 15°E, 0-20°N - land points only): a) Mean seasonal cycle, at each model's individual spatial resolution; b) Zonal
 539 mean of JJA precipitation, re-gridded to lowest common spatial resolution

540

541 **3.2. DeepMIP models' early Eocene simulations relative to preindustrial simulations and each**
 542 **other**

543 Here the focus is on mean precipitation differences between various DeepMIP early Eocene CO₂
 544 sensitivity experiments, in which all boundary conditions other than CO₂ were kept identical. The
 545 focus is not only on the precipitation response to varying CO₂ concentrations relative to the PI

546 simulations, but also from each CO₂ experiment individually (relative to each other). Precipitation
547 anomalies of all the CO₂ experiments versus PI are firstly briefly presented (Section 3.2.1), and then
548 the experiment results are divided into a CO₂ component (Section 3.2.2) and a non-CO₂ component
549 (i.e. the impact of the other boundary condition changes, Section 3.2.3).

550

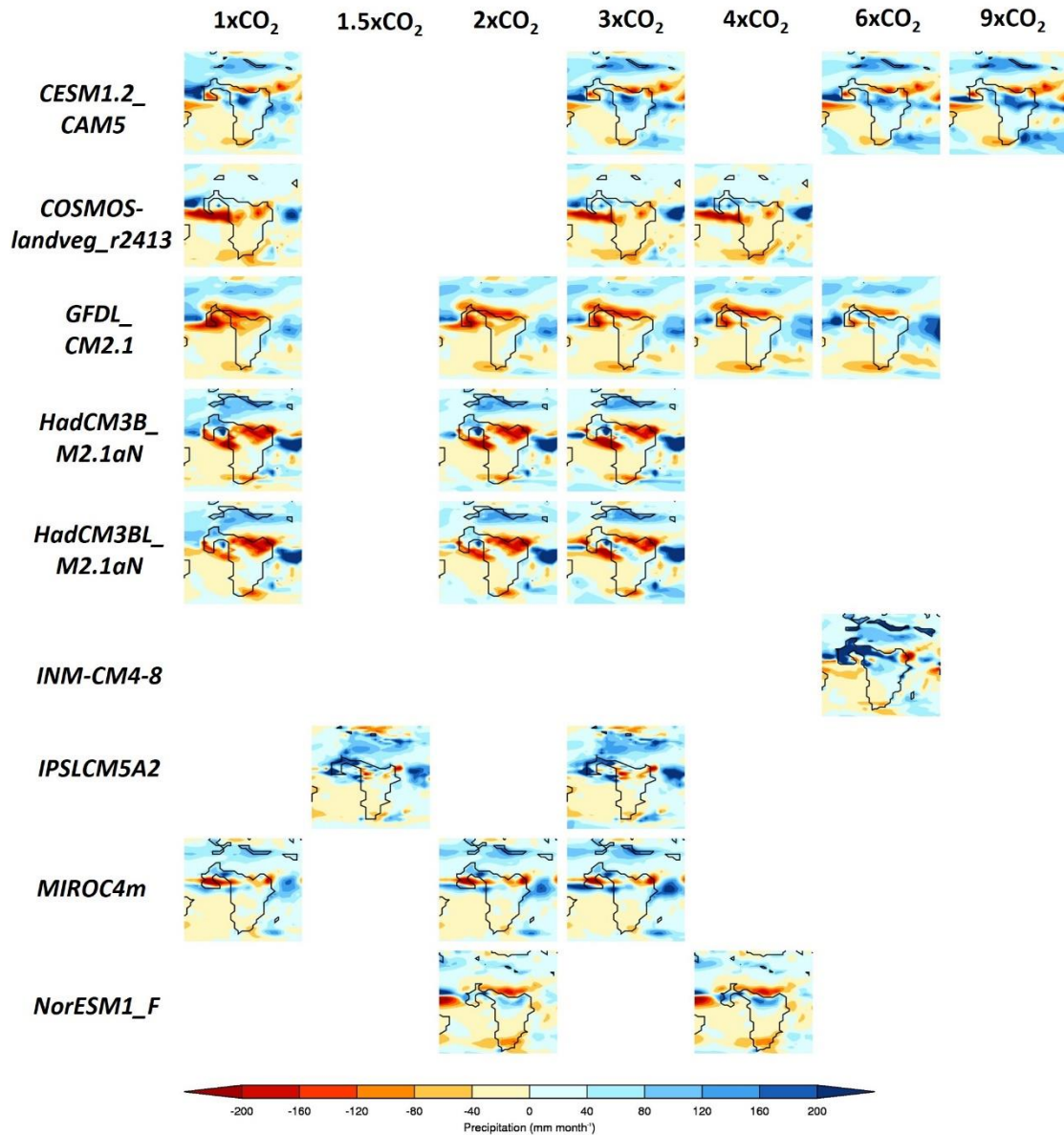
551 Before these results are presented, however, a brief introduction to the early Eocene precipitation over
552 Africa is needed. Mean JJA precipitation over PI and early Eocene Africa (using the 1x CO₂
553 simulation) is shown in the Supplementary Material, where it is clear that, during the PI, all models
554 are showing a band of precipitation between approximately the Equator and 10°N that extends from
555 the central equatorial Atlantic all the way across Africa (Figure S2a). How far east this rainbelt
556 extends is dependent on model, but the majority (and the MME) show it extending up to 40°E.
557 During the early Eocene, although this rain belt is still present over West Africa, most models agree
558 that it does not extend across the continent, instead ending at ~20°E and being replaced by relatively
559 drier conditions (Figure S2b). Wetter conditions are shown further east, over the early Eocene Indian
560 Ocean, but concerning Africa these results would suggest that although the rain belt is latitudinally
561 similar to the PI, it does not have the longitudinal extent.

562

563 ***3.2.1. All CO₂ experiments versus preindustrial***

564 The precipitation anomalies (early Eocene - PI), for each CO₂ experiment and for each model during
565 JJA are shown in Figure 4. This is only briefly presented, because the combination of a
566 palaeogeographic forcing and a CO₂ forcing makes interpretation difficult; this is why the results are
567 broken down into a CO₂ component and non-CO₂ component below. It should be noted that when the
568 MME is discussed below (see Sections 3.2.2 and 3.2.3), only models that participated in the particular
569 experiment are included.

570



571

572 Figure 4 - JJA precipitation climatology differences (early Eocene - PI), for each CO₂ simulation from each
 573 model

574

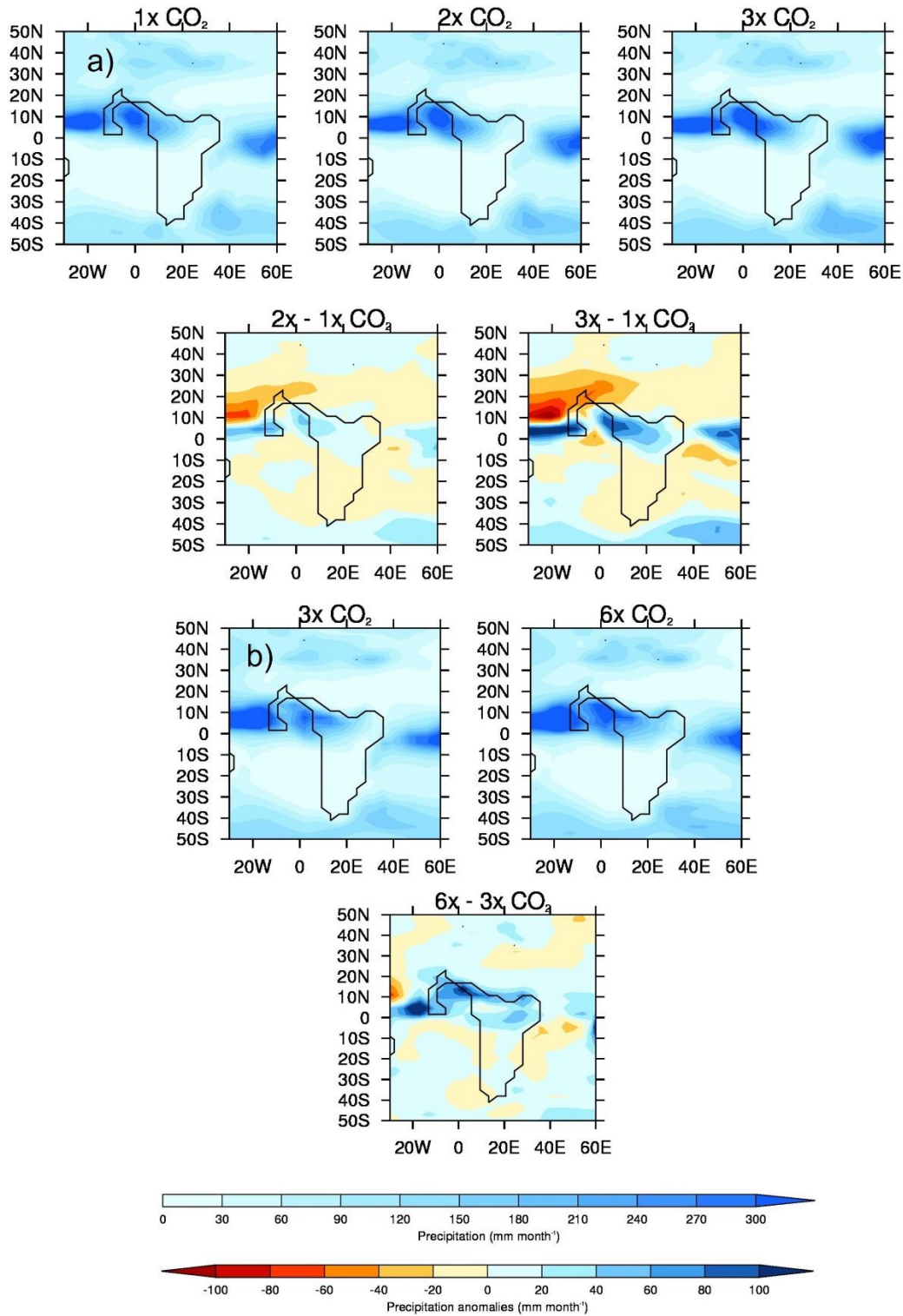
575 There is no clear linear trend in either wetting or drying across early Eocene Africa as the CO₂
 576 concentrations increase (Figure 4). Although many models show drying (relative to the PI) of up to
 577 ~180 mm month⁻¹ across northern and western Africa in the 1x, 2x and 3x experiments, this gradually
 578 disappears as higher CO₂ concentrations are applied, with some models showing precipitation
 579 increases of over 200 mm month⁻¹ (Figure 4). Some models disagree regardless of experiment, such
 580 as GFDL_CM2.1 which shows drying over northern Africa in all CO₂ experiments contrasting with
 581 IPSLCM5A2 which shows wetting over northern Africa in all CO₂ experiments. Further south, none
 582 of the models in any of the experiments are showing a large precipitation response. In very general
 583 terms, however, at the lower levels of CO₂ concentrations (i.e. up to 4x) the majority of models are
 584 showing the same region of drying over northern and western Africa.

585
586
587
588
589
590
591
592
593
594
595
596
597
598
599
600
601
602
603
604
605
606
607
608
609
610

3.2.2. Lower and higher CO₂ experiments: impact of CO₂

To investigate the impact of increasing CO₂ on precipitation, when all other boundary conditions are constant, the experiments have been divided into two samples, each containing a different number of models going into the MME: i) “lower-level CO₂”, namely the 1x, 2x and 3x experiments, comprising four models (GFDL_CM2.1, HadCM3B_M2.1aN, HadCM3BL_M2.1aN and MIROC4m); and ii) “higher-level CO₂”, namely the 3x and 6x experiments, comprising two models (CESM1.2_CAM5 and GFDL_CM2.1); see Table 1. Note that the MMEs for the two 3x experiments are slightly different because they contain a different number of models. Here, both absolute precipitation values and anomalies are shown, where the anomalies are of a certain CO₂ experiment versus another CO₂ experiment, rather than early Eocene versus PI.

The MME absolute precipitation and anomalies for the lower-level sample of CO₂ experiments, are shown in Figure 5a. When the absolute values are considered (Figure 5a, top row), all experiments show regions of precipitation maxima over the equatorial Atlantic (north of the Equator) and West Africa. Over the same West African region as described above (20°W-15°E, 0-20°N, land points only), mean JJA precipitation is 192 mm month⁻¹, 201 mm month⁻¹ and 207 mm month⁻¹ for the 1x, 2x and 3x experiments, respectively, implying a small increase as CO₂ increases. This becomes more evident when the anomalies are considered (Figure 5a, second row). If the 1x and 2x experiments are compared, the largest change is over the equatorial Atlantic, with a small increase in precipitation of up to 50 mm month⁻¹ over the Equator and a decrease of over 50 mm month⁻¹ further north, suggesting a southward displacement of the Atlantic ITCZ. Precipitation is also increased over western Africa. The same pattern is evident when the 1x and 3x experiments are compared, but more pronounced, with both the increases and decreases approaching 100 mm month⁻¹ in their respective areas.



611

612 Figure 5 – JJA precipitation multi-model ensemble mean (MME) climatologies and anomalies for the
 613 1x, 2x, 3x and 6x CO₂ experiments, using both samples: a) Lower-level sample of CO₂ experiments (comprising
 614 the four models that conducted these: GFDL_CM2.1, HadCM3B_M2.1aN, HadCM3BL_M2.1aN and
 615 MIROC4m), absolutes (top row) and anomalies (second row); b) Higher-level sample of CO₂ experiments
 616 (comprising the two models that conducted these: CESM1.2_CAM5 and GFDL_CM2.1), absolutes (top row)
 617 and anomalies (second row)

618

619 The MME absolute precipitation and anomalies for the higher-level sample of CO₂ experiments are
620 shown in Figure 5b. When the absolute values are considered (Figure 5b, top row), the region of
621 precipitation maxima in the equatorial Atlantic is larger in the 6x experiment. Over the same West
622 African region, mean JJA precipitation is 186 mm month⁻¹ and 232 mm month⁻¹ for the 3x and 6x
623 experiments, respectively, implying a large mean increase as CO₂ increases, and this is further
624 confirmed when the anomalies are considered (Figure 5b, second row). Precipitation increases of
625 over 100 mm month⁻¹ are shown over the equatorial Atlantic (north of the Equator) and West Africa
626 in the 6x relative to the 3x experiment, but the large region of drying seen at the lower levels of CO₂
627 is less evident (Figure 5b, second row). This suggests that, whilst West African precipitation is still
628 (and more so here) enhanced as CO₂ rises, it is perhaps less related to Atlantic ITCZ displacement and
629 more related to an increase in south-westerly flow (discussed further in Section 3.3).

630

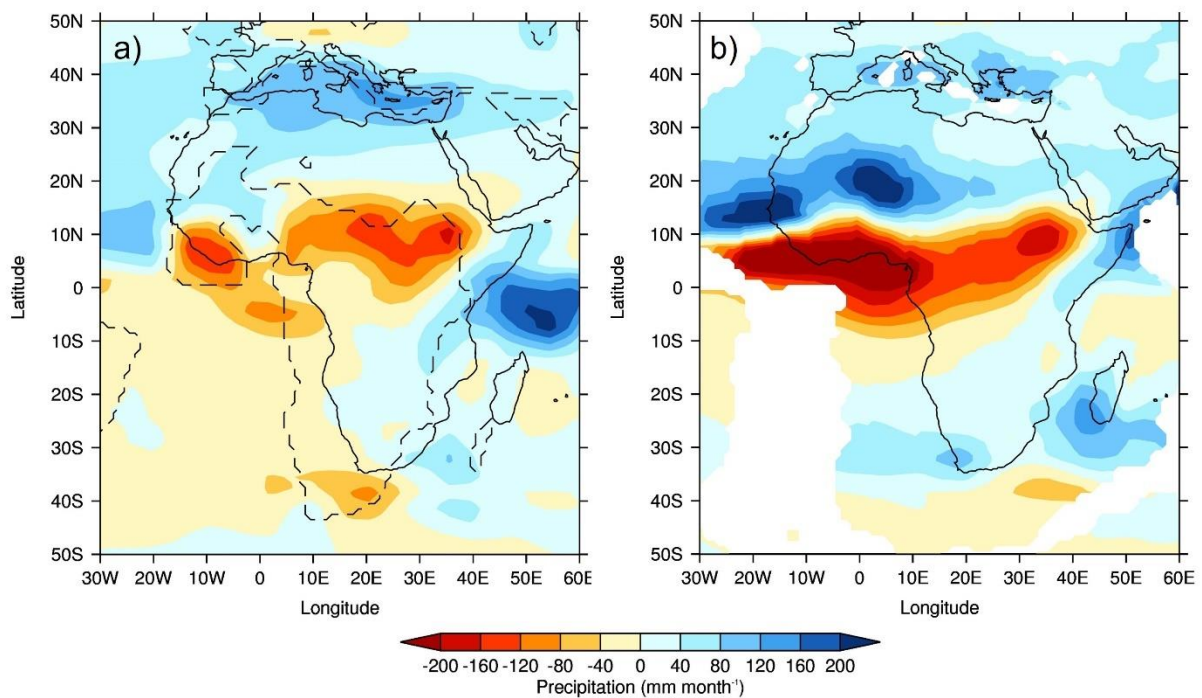
631 **3.2.3. 1x CO₂ experiment versus preindustrial: impact of non-CO₂ boundary conditions**

632 The 1x CO₂ experiment versus PI is of particular interest, because this shows the impact of the other
633 boundary conditions rather than that from CO₂ concentrations. When CO₂ concentrations are kept as
634 PI (as in the 1x experiment), the boundary conditions (see Section 2.1) likely to have the largest
635 impact on regional precipitation are the LSM, topography and vegetation (see Figure 1). Although
636 land ice changes, the largest of which during the early Eocene were over the Antarctic Ice Sheet
637 (AIS), do cause a precipitation response (e.g. Kennedy-Asser *et al.* 2019), this is thought to be a
638 mainly local signal and further afield, such as over northern and western Africa during JJA, there is
639 little or no precipitation change when the AIS is either imposed or removed (Kennedy-Asser, pers.
640 comm.).

641

642 The MME precipitation anomaly for this experiment is shown in Figure 6a; it should be noted that,
643 although six models conducted this experiment (CESM1.2_CAM5, COSMOS-landveg_r2413,
644 GFDL_CM2.1, HadCM3B_M2.1aN, HadCM3BL_M2.1aN and MIROC4m), only the latter four are
645 included here in the MME, to be consistent with the analysis of the CO₂ component (Section 3.2.2).
646 From the available DeepMIP results, it is impossible to disentangle the boundary conditions and
647 ascertain which is dominant in causing the precipitation response; in an ideal world, sensitivity
648 experiments would be conducted to introduce each boundary condition individually, but this is not
649 possible with the results currently available on the DeepMIP database. Nevertheless, based on the
650 results it is possible to theorise which of these boundary conditions might be causing this MME
651 precipitation response. The largest precipitation changes relative to the PI are a small increase in
652 precipitation to the north of early Eocene Africa and in the western Indian Ocean, and a decrease in
653 precipitation over western and northern equatorial Eocene Africa (Figure 6a). It is likely that the
654 northern increases are caused by the change in the LSM (Figure 1a) as this region comprises the
655 preindustrial (and modern) Sahara but is ocean in the early Eocene and therefore would have been a

656 much greater moisture source. Likewise, the increase over the western Indian Ocean is likely because
 657 preindustrial Africa extends much further East than during the early Eocene, again giving much less
 658 of a moisture source during the PI (Figure 1a). Moreover, an examination of SST from the early
 659 Eocene and PI simulations (from each individual model and the MME) shows that these exposed
 660 regions of ocean are characterised by warmer SSTs in the early Eocene; for example, in the Indian
 661 Ocean absolute values are up to 32°C in the early Eocene MME compared to up to 28°C in the PI
 662 MME, thereby providing a greater source of evaporation during the Eocene see (see Supplementary
 663 Material, Figure S3). Concerning the drying over equatorial early Eocene Africa, this is more
 664 difficult to interpret and does not seem likely to be related to the LSM or the changes in vegetation.
 665 For the LSM, this region of drying coincides with land during both time periods. For the vegetation,
 666 although there is a shift in biome between the PI and early Eocene, the region of drying (at
 667 approximately 10-20°N) coincides with an increase (or slightly northward shift) in tropical rainforest
 668 during the early Eocene, rather than mostly being savanna and grassland in the PI (Figure 1c). This
 669 might be expected to result in an increase in precipitation during the early Eocene, rather than a
 670 drying. However, this response might be explained by the difference in orographic heights over this
 671 region (i.e. over central equatorial Africa), where early Eocene Africa is considerably lower (up to
 672 400 m) than in the PI (up to 1000 m). Finally, over southern Africa, although there is a large increase
 673 in orographic heights (of over 1000 m) during the early Eocene (Figure 1b and Figure S1 in the
 674 Supplementary Material), this does not appear to be having a large impact on African precipitation,
 675 with minimal precipitation differences in the south (Figure 6a).



676
 677 Figure 6 – JJA precipitation multi-model ensemble mean (MME) climatology differences (early Eocene - PI) for
 678 the 1x CO₂ experiment (comprising the four models that conducted this experiment, in addition to the others

679 considered here: GFDL_CM2.1, HadCM3B_M2.1aN, HadCM3BL_M2.1aN and MIROC4m): a) Original (i.e.
680 unrotated) differences; b) Rotated differences i.e. Charlie Eocene precipitation rotated forward to where it is in
681 the PI. Note that in a), solid lines show the PI mask and dashed lines show the Eocene mask.

682

683 However, a caveat of the above analysis is that, because of the plate rotation differences during the
684 early Eocene, Figure 6a is showing precipitation anomalies that may simply be due to differing
685 geographical locations, rather than any change to the climate state. Therefore, Figure 6b shows the
686 same results, but this time with the early Eocene precipitation rotated forwards (based on the rotations
687 supplied in the Herold *et al.* 2014 Supplementary Material) to where it is in the PI. However, despite
688 these rotational differences, the overall picture remains the same (i.e. increases in precipitation over
689 northern Africa and a decrease in precipitation over western and equatorial Africa) but much more
690 pronounced (Figure 6b). The increases and decreases in precipitation exceed 200 mm month⁻¹ in
691 some places, suggesting a northward displacement of the Atlantic ITCZ; this difference between the
692 early Eocene and the PI is in contrast to when the Eocene CO₂ experiments are compared with each
693 other, to assess the impact of increasing CO₂ (discussed previously in Section 3.2.2).

694

695 **3.3. Physical mechanisms behind the precipitation response**

696 Here the focus is on the possible dynamic and thermodynamic mechanisms causing the observed
697 precipitation responses, again using the MME absolute values and anomalies from the aforementioned
698 lower-and higher level samples of CO₂ experiments.

699

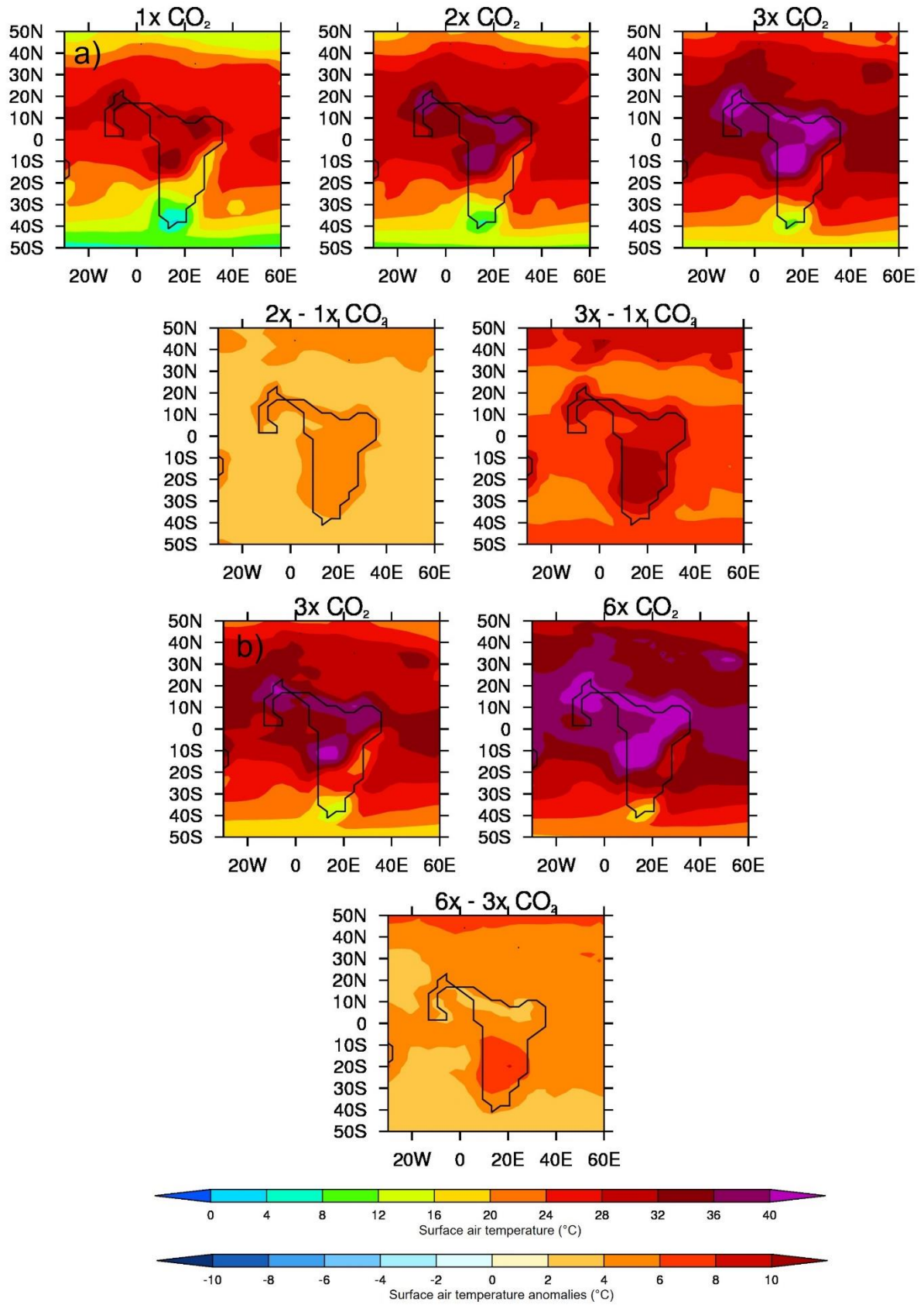
700 The MME absolute 1.5 m surface air temperature (SAT) and anomalies for the lower- and higher-
701 level sample of CO₂ experiments are shown in Figure 7. In line with general understanding there is a
702 clear increase in absolute SAT, everywhere, as the CO₂ increases, with the largest signal (of up to
703 40°C in the 3x experiment) occurring over the main landmass of central and northern Africa (Figure
704 7a, top row). This is more obvious when the anomalies are considered, although the largest increases
705 are occurring further south (Figure 7a, second row). This is even more pronounced in the higher-level
706 sample of CO₂ experiments (Figure 7b), and in all experiments the largest increase in SAT, either
707 between the 3x and 1x experiments or the 6x and 3x the experiments, is occurring over southern
708 Africa, away from the largest precipitation changes discussed above. Moreover, the largest increases
709 in precipitation as CO₂ increases (Figure 5) are shown over ocean regions, such as the equatorial
710 Atlantic and off the coast of West early Eocene Africa, whereas the largest increases in SAT (Figure
711 7) are shown over the landmass. It is likely that these precipitation increases are connected to the
712 warmer SSTs (see Section 3.2.3), or changes to the low-level circulation (discussed below), rather
713 than a direct response to the heating landmass. The Precipitation - Evaporation (P-E) balance (Figure
714 8) is positive over West Africa in all experiments regardless of sample, corresponding well with the
715 region of increased precipitation (Figure 6), as does cloud cover which is also increasing with CO₂

716 over these regions (not shown). Further south, over the Atlantic, the balance is negative implying
717 increased evaporation corresponding to the increased oceanic SAT. Concerning low level circulation,
718 as shown by 850 mb vector winds (Figure 9), when the anomalies are considered (and in particular the
719 3x versus 1x), there is a small (of up to 5 ms^{-1}) increase in northerly and westerly winds (i.e.
720 clockwise flow) in the equatorial Atlantic north of the Equator (Figure 9a, second row). However, in
721 the higher-level CO_2 sample (and in particular the anomalies of 6x versus 3x, Figure 9b, second row),
722 this increase in anticyclonic flow is less evident and is instead replaced by a widespread area of
723 increased southwesterly flow across most of the equatorial Atlantic and central Africa. For SAT, P-E
724 and 850 vector winds from each individual model, rather than the MME, see the Supplementary
725 Material (Figure S4a, b, and c, respectively); here, similar to Figure 4, there is no obvious linear
726 change in either P-E or low level circulation as CO_2 increases, but a clear increase in SAT from all
727 models, in line with current understanding (Figure S4a).

728

729 Both the region of enhanced precipitation over West Africa, and the region of drying in the equatorial
730 Atlantic around 10°N , may be explained by these low-level circulation changes. Up to 3x that of the
731 PI CO_2 , clockwise low-level circulation increases with CO_2 , drawing in more moisture from the
732 equatorial Atlantic and causing a relative drying further north, hence the appearance of a southward
733 displacement of the Atlantic ITCZ. At higher levels of CO_2 , however, where increases in West
734 African precipitation are shown but the region of drying around 10°N is not, the increased clockwise
735 low-level circulation is replaced by increased south-westerly flow; here, therefore, precipitation is
736 being enhanced by more moisture being drawn in by this south-westerly flow from the warm South
737 Atlantic.

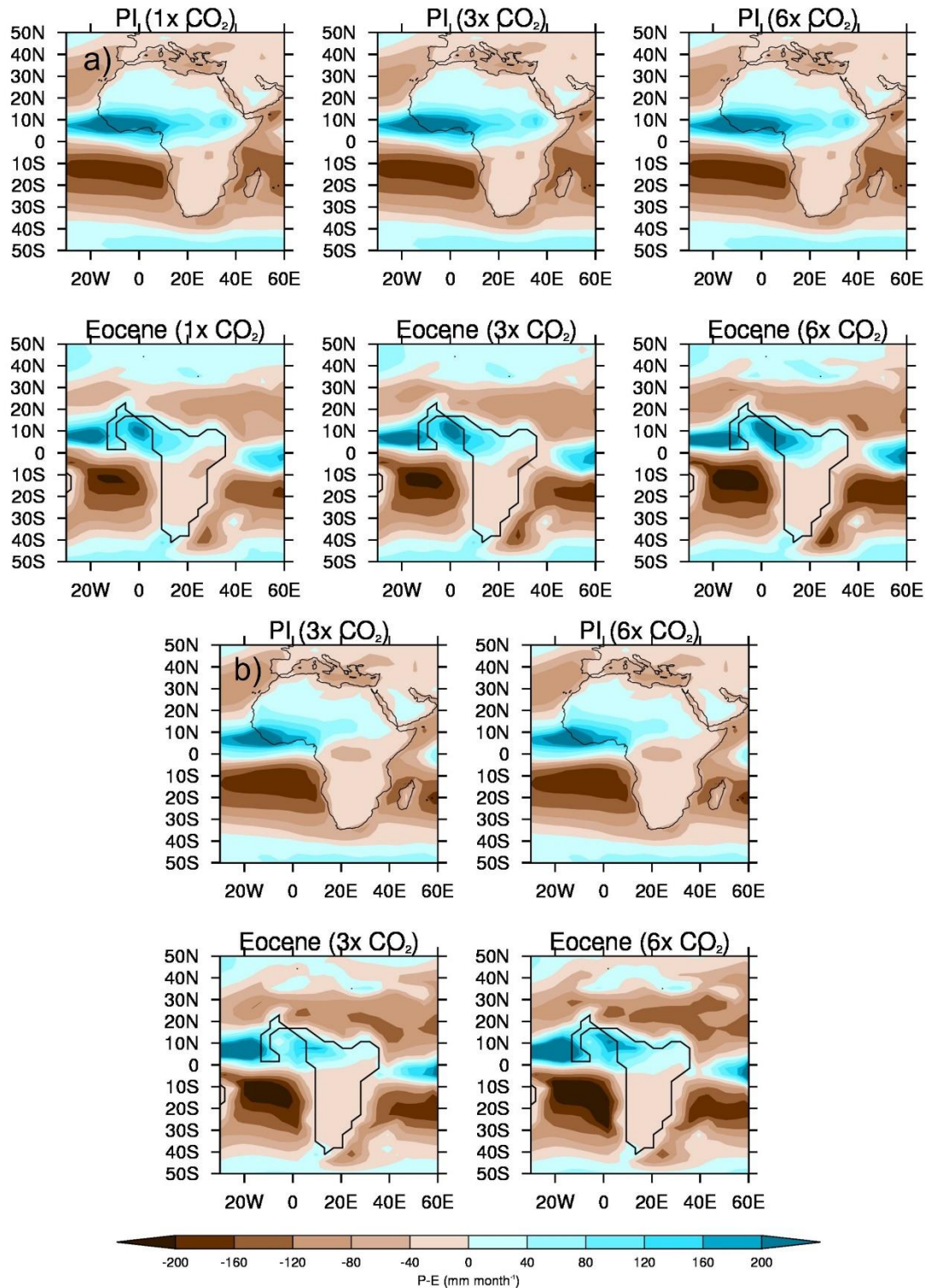
738



739

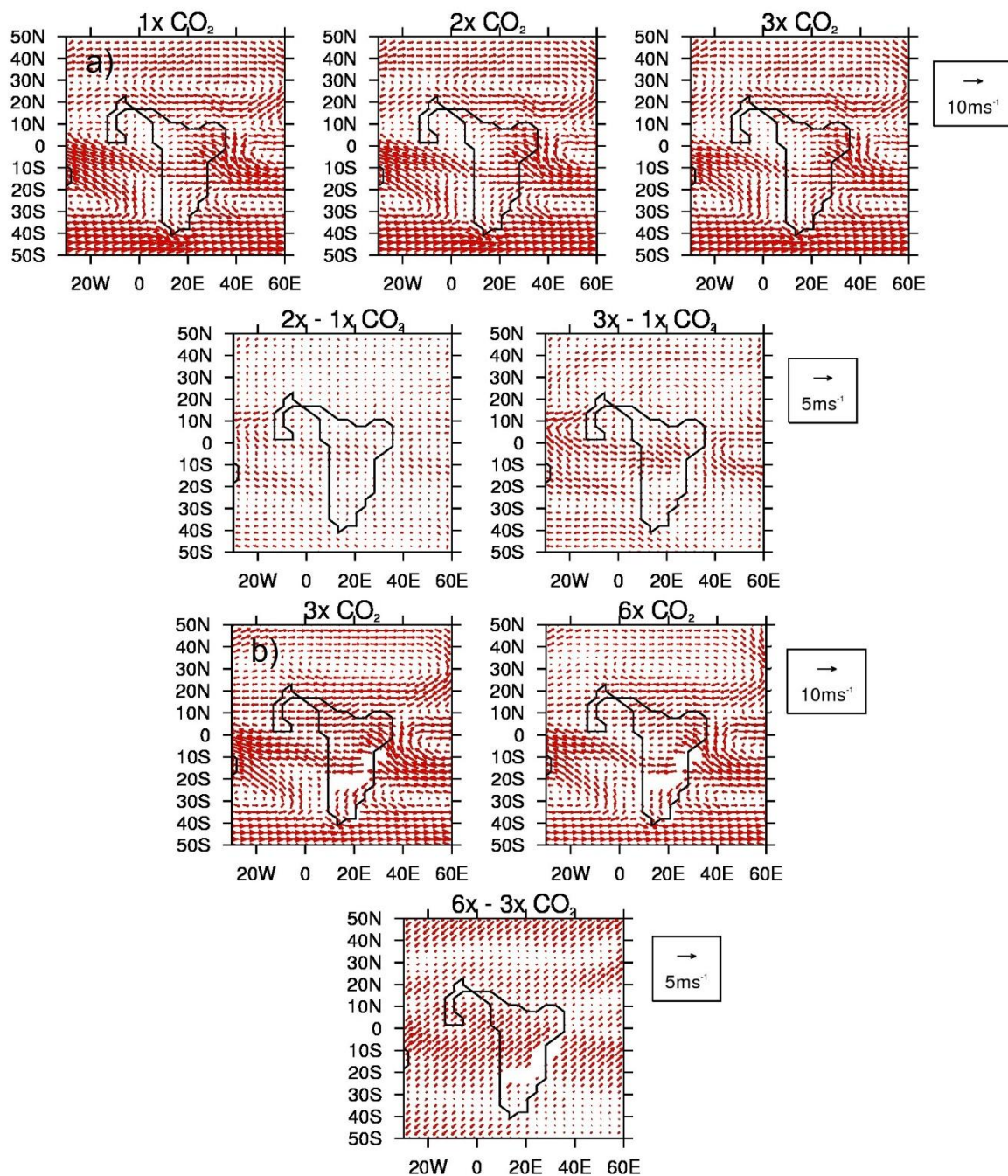
740 Figure 7 – Same as Figure 5 but for JJA 1.5 m surface air temperature

741



742

743 Figure 8 – JJA P-E multi-model ensemble mean (MME) climatology absolutes for the 1x, 2x, 3x and 6x CO₂
 744 experiments, using both samples: a) Lower-level sample of CO₂ experiments (comprising the four models that
 745 conducted these: GFDL_CM2.1, HadCM3B_M2.1aN, HadCM3BL_M2.1aN and MIROC4m), PI (top row) and
 746 early Eocene (bottom row); b) Higher-level sample of CO₂ experiments (comprising the two models that
 747 conducted these: CESM1.2_CAM5 and GFDL_CM2.1), PI (top row) and early Eocene (bottom row). Note that
 748 the PI panels are identical in each sample because they contain the same models, but are simply replicated here
 749 for ease of comparison



751

752 Figure 9 – Same as Figure 5 but for JJA 850 mb wind

753

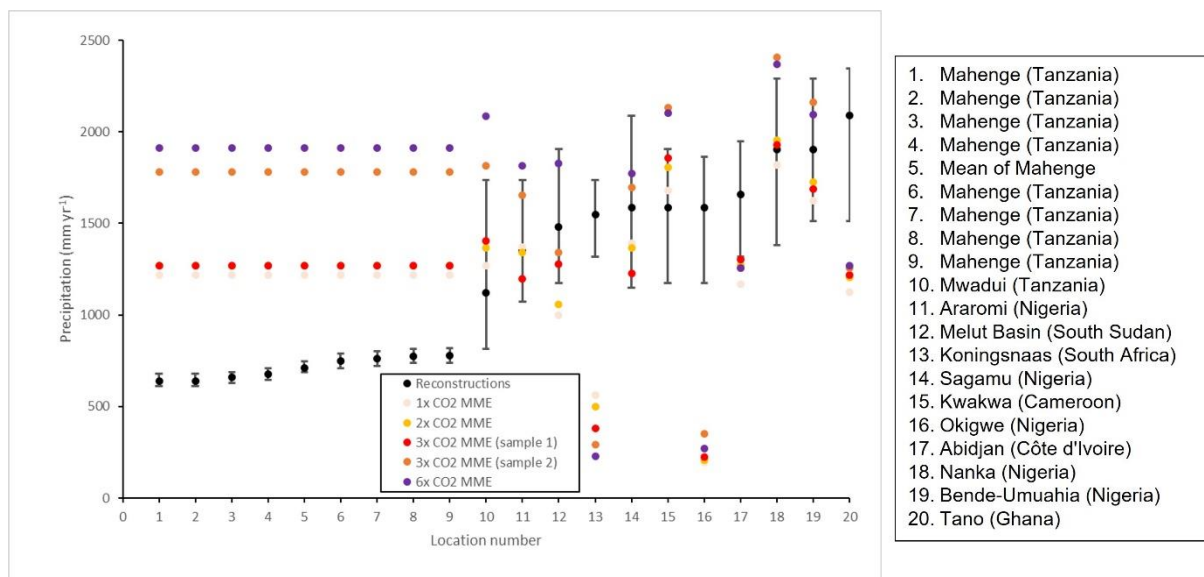
754 **3.4. DeepMIP models' Eocene simulations versus proxy data**

755 In this final section, the focus is on comparing precipitation from selected DeepMIP early Eocene
 756 simulations (using the MME from the same two samples as discussed above) with newly-available
 757 precipitation reconstructions (described in Section 2.3.2). Before the results are presented, however,
 758 several sources of uncertainty in the proxies and models must be noted, aside from analytical
 759 uncertainty that is expressed in the reconstructed confidence intervals. Firstly, the fossil plant
 760 assemblages analysed here have broad age constraints. Palaeofloral assemblages may capture a

761 snapshot within those age constraints that deviated climatically from the average climatic conditions
762 of a specific age that the model was calibrated on. In addition, fossil plant assemblages tend to
763 preserve better in wetter climates, with drier climates lacking the water bodies needed to preserve
764 plant fossils. Secondly, the DeepMIP models are calibrated on atmospheric CO₂ proxy
765 reconstructions to cover the uncertainty of the entire Eocene; the lower CO₂ levels may be more
766 representative of the late Eocene, but that was not the purpose or interpretation when it came to
767 deciding the experiments. Independent proxies within those ages produce widely variable
768 atmospheric CO₂ reconstructions (e.g. Rae *et al.* 2021), with <500 ppmv from some palaeosol and
769 stomatal reconstructions (Beerling *et al.* 2009; Hyland *et al.* 2013) to >2000 ppmv from boron
770 isotopes and alkenone $\delta^{13}\text{C}$ (e.g. Bijl *et al.* 2010; Anagnostou *et al.* 2020). It should be noted,
771 however, that there is high uncertainty in these reconstructions; see Hollis *et al.* (2019) for a full
772 discussion. For example, based on a variety of reconstructions compiled as part of the Palaeo-CO₂
773 project (including phytoplankton, boron proxies, leaf gas exchange, liverworts and nahcolite),
774 atmospheric CO₂ during 55-50 Ma ranges from 500-2000 ppmv (Anagnostou *et al.* 2020, Hollis *et al.*
775 2019, Westerhold *et al.* 2020). Potentially, these differences in reconstructed atmospheric CO₂ reflect
776 transient climate states (e.g. Reichgelt *et al.* 2016), but regardless, the disagreement between proxy
777 reconstructions makes it problematic to associate a single atmospheric CO₂ level for model-data
778 comparison (Hollis *et al.* 2019). Lastly, a major source of uncertainty is the paucity of proxy data
779 across Africa; as mentioned above, even today there is a lack of long-term climate data over much of
780 Africa, and the same is true for palaeofloras. This sparsity, therefore, is likely responsible for some of
781 the results discussed below, and this is why some of the following results are necessarily partly
782 speculative.

783

784 With these caveats in mind, MME MAP at each of the individual locations is shown in Figure 10,
785 ordered according to the reconstructions' values, including uncertainty estimates for the
786 reconstructions (as measured by +/- 1 standard deviation for the locations in Mahenge, Tanzania and
787 the 95% confidence interval for the other 11 locations; see Table 2 for details). The approximate
788 geographical locations can be seen in the Supplementary Material (Figure S5). Firstly it is worth
789 noting that for the majority of reconstructions, uncertainty is high, with a range of up to +/- 1000 mm
790 yr⁻¹ at some of the locations such as Mwadui, Tanzania (Figure 10). Secondly, whether or not the
791 CO₂ experiments over- or underestimate MAP appears to depend heavily on geographical location,
792 with none of the CO₂ experiments (not even the 6x experiment) reproducing the precipitation amounts
793 of the proxy reconstructions in some locations, such as Koningsnaas, South Africa, Okigwe, Nigeria
794 or Tano, Ghana (Figure 10). Elsewhere, the simulations lie within the uncertainty range of the
795 reconstructions (such as Sagamu or Bende-Umuahia, both in Nigeria), and yet in other places (such as
796 across Kwakwa, Cameroon, and all of the locations at Mahenge, Tanzania) all of the simulations are
797 too wet, by between ~760-1040 mm year⁻¹ depending on location and CO₂ experiment (Figure 10).

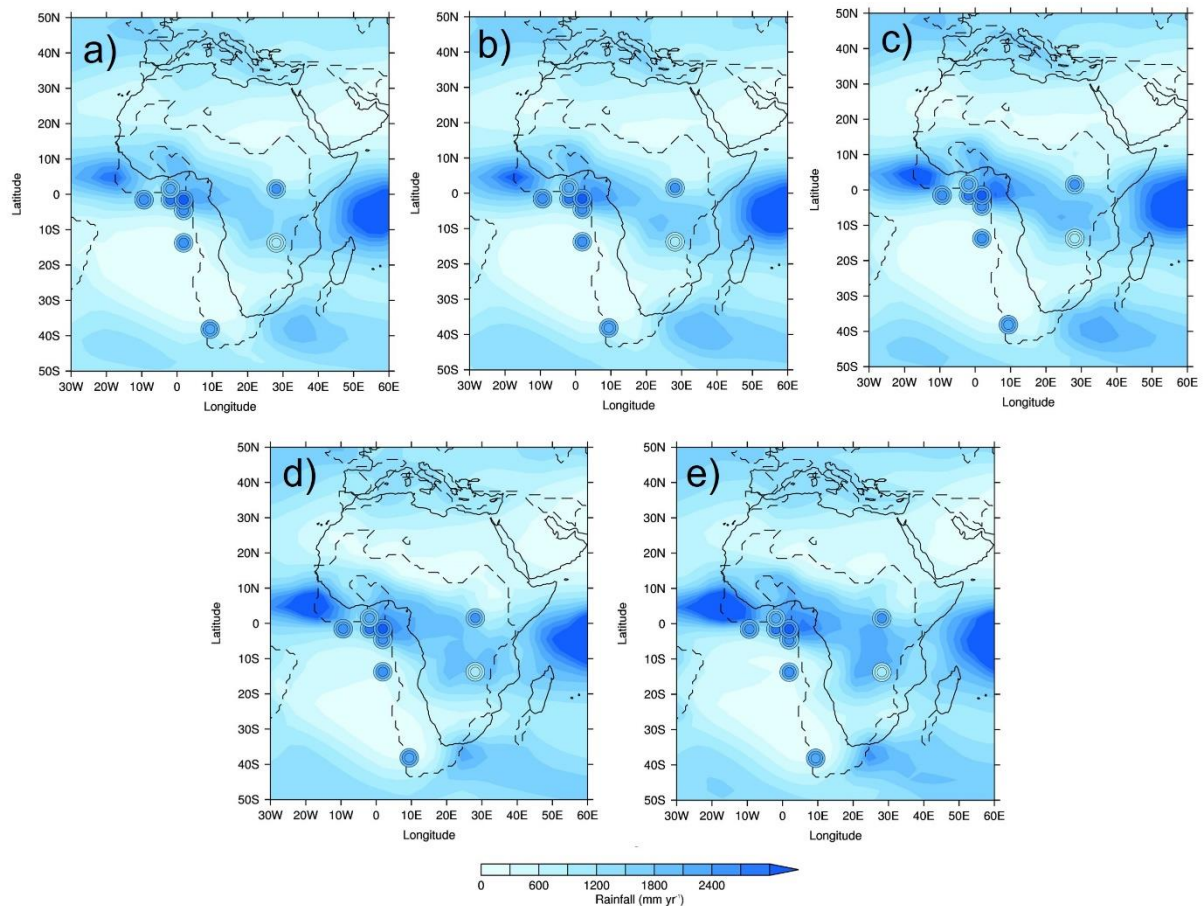


799

800 Figure 10 – Annual mean precipitation from reconstructions (black) and CO₂ experiments multi-model
 801 ensemble mean (MME, colours) at each individual location. Uncertainty in reconstructions is measured by 95%
 802 confidence interval for all sites except Mahenge, where they show +/- 1 standard deviation. Locations have
 803 been ordered according to the reconstructions' values, lowest to highest. Note that locations 1-4 and 6-8 are all
 804 in the same location, but from different stages during the Lutetian (~41-47 Ma), and so have been re-sampled
 805 and averaged into one overall mean (location 5)

806

807 Spatially, MME MAP is shown in Figure 11 (see Figure S6 in the Supplementary Material for each
 808 individual model), showing the uncertainty estimates as concentric circles. As already discussed, the
 809 simulations' precipitation is clearly too high or too low compared to proxy reconstructions in different
 810 parts of Africa. Qualitatively, in very general terms all of the CO₂ experiments are showing wetter
 811 conditions over Western early Eocene Africa (relative to elsewhere), agreeing with Figure 10 where in
 812 many of these locations the models are either within, or at the higher end of, the reconstructions'
 813 uncertainty ranges (Figure 11). Importantly, simulated precipitation over West Africa appears to be
 814 increasing as the CO₂ concentration increases and, in particular for the 6x experiment (Figure 11e), in
 815 this region simulated precipitation exceeds even the upper range of uncertainty of the reconstructions.



816

817 Figure 11 – Annual mean precipitation from reconstructions (circles) and CO₂ experiments multi-model
 818 ensemble mean (MME, background gridded data): a) 1x; b) 2x; c) 3x (lower-level CO₂ sample); d) 3x (higher
 819 level CO₂ sample); e) 6x. Concentric circles show 95% confidence interval for all sites except Mahenge, where
 820 they show +/- 1 standard deviation: outer circle = lower range (or -1 standard deviation), middle circle = average
 821 (or, for Mahenge, mode) and inner circle = upper range (or +1 standard deviation). Reconstructions have been
 822 rotated forwards to where they are in the PI. Solid lines show the PI mask and dashed lines show the early
 823 Eocene mask. Note that, using the common spatial resolution of the MME, 3 reconstructions are all in the same
 824 location in West Africa (even though they are in different locations in reality); here, therefore, only the top-most
 825 reconstruction is shown

826

827 Quantitatively, the root mean squared error (RMSE) between each model (as well as the MME) and
 828 the reconstructions at every location is shown in Table 3 and, similar to the anomalies from each
 829 model as discussed above, there is no clear relationship between changing CO₂ and a better match to
 830 the reconstructions. Most models suggest a better fit to the reconstructions at lower levels of CO₂,
 831 such as CESM1.2_CAM5 where there is a general increase in RMSE as the CO₂ increases; however,
 832 this is not the case for every model, with for example GFDL_CM2.1 showing a better fit with
 833 reconstructions at 2x and 4x CO₂, rather than higher or lower levels (Table 3). For many of the
 834 models and the MME, the 3x CO₂ experiments are showing the least fit with reconstructions. The
 835 MME, from the lower-level (but not in the higher-level) CO₂ sample, agrees with this conclusion that

836 lower CO₂ is giving a slightly better match to the reconstructions, with RMSE values of 758 mm year⁻¹, 831 mm year⁻¹, 1385 mm year⁻¹, 889 mm year⁻¹ and 839 mm year⁻¹ for the 1x, 2x, 3x (lower-level
 837 CO₂ sample), 3x (higher-level CO₂ sample) and 6x experiments, respectively (Table 3).
 838

839

	1x CO ₂	1.5x CO ₂	2x CO ₂	3x CO ₂	4x CO ₂	6x CO ₂	9x CO ₂
CESM1.2_CAM5	681			750		704	822
COSMOS-landveg_r2413	699			1424	713		
GFDL_CM2.1	803		762	1027	786	975	
HadCM3B_M2.1aN	796		884	1988			
HadCM3BL_M2.1aN	816		1018	1742			
INM-CM4-8						966	
IPSLCM5A2		744		669			
MIROC4m	614		662	785			
NorESM1_F			1149		1522		
MME (lower-level CO₂ sample)	758		831	1385			
MME (higher-level CO₂ sample)				889		839	

840

841 Table 3 - Root Mean Squared Error (RMSE) for mean annual precipitation (MAP) between each model (and
 842 multi-model ensemble mean, MME, using both samples) and reconstructions, for each CO₂ experiment
 843

844 4. DISCUSSION AND CONCLUSIONS

845 This study has investigated African precipitation during the early Eocene, as simulated by the
 846 DeepMIP models. This study is novel, because it investigates the relatively little-studied subject of
 847 African hydroclimate during the early Eocene. The results of this study have been divided into four
 848 separate sections, corresponding to the four questions posed in Section 1. Firstly, in Section 3.1 the
 849 DeepMIP models' PI simulations have been compared to satellite-derived estimates of precipitation,
 850 to ascertain how well the models are able to reproduce African precipitation under 'modern'
 851 conditions (please see Section 2.3.1 for a discussion of the caveat that here the term 'modern' is
 852 actually a combination of both pre-industrial and 20th-21st century). Secondly, in Section 3.2 the
 853 DeepMIP models' early Eocene simulations have been compared to both the PI simulations and each
 854 other, to investigate the impact of CO₂ components (i.e. increasing CO₂) and non-CO₂ components
 855 (i.e. other boundary condition changes, such as to the LSM) on African precipitation. Thirdly, in
 856 Section 3.3 the CO₂ driven response has been investigated further by looking at a number of dynamic
 857 and thermodynamic fields simulated by the models, to ascertain possible physical mechanisms behind
 858 the observed precipitation response. Lastly, in Section 3.4 the DeepMIP models' early Eocene
 859 simulations have been compared to newly-available proxy data, to indicate how well the models agree
 860 with current best precipitation estimates from the Eocene.

861
862 The comparison between the DeepMIP PI simulations and modern observations (from TAMSAT)
863 suggest that individual models are both underestimating or overestimating the spatial patterns of
864 African precipitation; this is consistent with Monerie *et al.* (2020), who analysed a number of
865 historical simulations from both CMIP5 and CMIP6 and found that the models' ability to reproduce
866 observations was firstly model dependent and secondly geographically dependent, with many models
867 underestimating precipitation over the Sahel and overestimating it over the Guinea coast and tropical
868 Atlantic. However, here the MME is reducing these biases and is showing the best agreement with
869 TAMSAT in terms of precipitation spatial patterns, highlighting the utility of the MME as a best
870 estimate of the actual precipitation. This has been found elsewhere, such as by Ayugi *et al.* (2021)
871 who looked at East African precipitation in both CMIP5 and CMIP6 models and again found a better
872 performance of the MME relative to individual models, due to systematic errors in individual models
873 being cancelled out. Moreover, Rougier *et al.* (2013) show that it is actually a statistical property of
874 this type of analysis that the ensemble mean will always provide the best match to the data e.g. have
875 the lowest RMSE. It should be noted, however, that a potential caveat of using the MME is that
876 although it eliminates extreme biases, the same models are then being used to run the Eocene
877 simulations, for which the correct (i.e. true) precipitation is less well known and based only on
878 palaeodata, which themselves have uncertainties. Therefore, even using the MME may be
879 propagating its own unknown errors. Concerning the latitudinal extent and seasonal timings of
880 African precipitation, most models show a much wider (latitudinally) West African rain belt
881 compared to TAMSAT and are not reproducing the rapid drop-off in precipitation near the Equator or
882 north of 15°N. This is somewhat in contrast to Monerie *et al.* (2020), who noted that the majority of
883 CMIP5 and CMIP6 models did not have the monsoon extending far enough to the north and were
884 instead showing a southward displacement of precipitation maxima, relative to observations; however,
885 that particular study used the models' historical simulations (as well as a different MME), not pre-
886 industrial as shown here, which may explain the discrepancy. Outside of JJA most models are too
887 wet, but within JJA the results suggest that the drier models (i.e. those underestimating African
888 precipitation) are closer to modern observations than those that are too wet (i.e. overestimating
889 African precipitation).

890
891 The comparison between the DeepMIP early Eocene simulations and the PI suggests that, when all
892 individual models are considered separately, there is no obvious wetting or drying trend (relative to
893 the PI) as the CO₂ increases. This is another reason to focus on the MME, which allows easier
894 interpretation as the large model spread is removed. Concerning the non-CO₂ component of
895 precipitation change (i.e. the impact of other boundary conditions when CO₂ is kept at PI levels), the
896 results suggest that changes to the LSM may be responsible for the increases in precipitation (relative
897 to the PI) to the north of early Eocene Africa and the western Indian Ocean, given that these are

898 ‘newly exposed’ regions of ocean in the early Eocene, thereby providing a larger moisture source. In
899 contrast, it is likely that changes in orographic heights are responsible for the region of drying
900 (relative to the PI) over equatorial early Eocene Africa, where early Eocene Africa is considerably
901 lower (up to 400 m) than in the PI (up to 1000 m). When the early Eocene precipitation is rotated
902 forwards in time to where it is in the PI, a similar pattern is shown but is more pronounced, and
903 suggests a northward displacement of the primary rain belt (relative to today), which is consistent
904 with previous work (e.g. Carmichael *et al.* 2016). Concerning the CO₂ component of precipitation
905 change, at the lower levels of increased CO₂ (such as 2x and 3x that of the PI) precipitation over the
906 equatorial Atlantic and West Africa appears to be increasing in response to rising CO₂, with the
907 concomitant decrease in precipitation north of the equator suggesting a possible displacement of the
908 Atlantic ITCZ towards the south. This therefore suggests that the boundary condition changes
909 imposed for the Eocene are resulting in a northward displacement of the primary rain belt, but
910 increasing CO₂ (with the same boundary conditions) is resulting in a southward displacement of the
911 primary rain belt. At even higher levels of CO₂ (such as 6x that of the PI), precipitation over West
912 Africa is more enhanced relative to the lower levels, but the region of drying is less evident. The
913 enhancement of Northern Hemisphere summer West African precipitation at the highest levels of CO₂
914 is again consistent with previous work, such as that of Carmichael *et al.* (2016) who showed a
915 generally more intense hydrological cycle at higher CO₂ levels and that of Carmichael *et al.* (2018)
916 who demonstrated an increase in precipitation extremes over tropical Africa at higher CO₂ levels.
917

918 Consistent with Carmichael *et al.* (2016), the precipitation increases over West Africa as CO₂
919 concentrations rise are associated with increased SAT, a strongly positive the P-E balance and cloud
920 cover increases and, concerning temperature, as such are consistent with the idea that a generally
921 warmer world results in a generally wetter world; the ‘wet-gets-wetter and dry-gets-drier’ hypothesis
922 (e.g. Held and Soden 2006). However, the largest increases in SAT shown here are over southern
923 Africa, not where the largest precipitation increases are seen, suggesting factors other than a generally
924 warming world (i.e. dynamical changes) are responsible for the localised precipitation response (see
925 Section 3.3). A caveat to mention here is that, because the DeepMIP simulations use prescribed
926 vegetation rather than interactive, there is no impact on the vegetation types or distribution of these
927 enhanced SATs or precipitation, therefore it is not possible to say whether any enhanced precipitation
928 would be enough to support a certain type of vegetation in the presence of extreme temperatures.
929 Whilst it is likely that the impacts of elevated temperatures and precipitation (whether combined or
930 individually) would be substantial on plant physiology, it is beyond the scope of this study to test this.
931 Sensitivity studies, using interactive vegetation, are currently underway to address these questions.
932

933 Lastly, the results from the model-data comparison suggests that whether the early Eocene
934 simulations (regardless of CO₂ experiment) over- or underestimate African precipitation is highly

935 geographically dependent, with some of the CO₂ experiments at some of the locations lying within the
936 uncertainty range of the reconstructions but others being too wet or too dry. There is some suggestion
937 of a latitudinal relationship, with the simulations overestimating precipitation near the Equator and
938 underestimating precipitation in high latitude regions, such as South Africa; this latter point is
939 consistent with the findings of Carmichael *et al.* (2016). Whether the models are considered
940 independently or whether the MME is used, the results suggest a marginally better fit with the
941 reconstructions at lower levels of CO₂, and this is in contrast (indirectly) to the findings of Carmichael
942 *et al.* (2016) who suggested the warmest models in the regions of increased precipitation best matched
943 the data; it should be noted, however, that this was a global study. There is no evidence for this here,
944 and indeed the finding of a better match at lower levels of CO₂ is in contrast to that of Reichgelt *et al.*
945 (2021, in prep) who focused on Australia and found that the higher, 6x CO₂ experiment was the best
946 match to reconstructions. However, given the uncertainties associated with both the reconstructions
947 (discussed above) and the boundary conditions used to force the models, it is difficult to draw firm
948 conclusions from a model-data comparison of this type. Moreover, a particularly big problem is that,
949 despite the newly-compiled reconstructions presented here, there is still a lack of data across Africa,
950 hindering any firm conclusions. The uncertainties discussed above are likely contributing to the lack
951 of consistency presented in some of these model-data comparisons, such as the MME showing better
952 agreement with the reconstructions at lower and higher levels of CO₂, but not in between (e.g. the 3x
953 simulation), but this is, at present and given the data sparsity, unavoidable.

954

955 In conclusion, therefore, this study has shown that the DeepMIP models are able to approximately
956 reproduce the modern African precipitation and, in response to rising CO₂, suggest an enhancement of
957 precipitation in this region associated with increasing temperatures and changes to low-level
958 circulation. At very high levels of CO₂ the models may be too wet, relative to proxy reconstructions.
959 However, this might be because the NLR proxy approach has difficulty generating MAP values above
960 modern, or connected to the relatively few early Eocene-aged data points within the reconstructions
961 (meaning some of the comparisons here were necessarily made with data from the middle or late
962 Eocene). Using the MME provides the clearest suggestion of this, but the large amount of model
963 spread means that when individual models are considered, either relative to their corresponding PI
964 simulations or reconstructions, no clear relationship is shown.

965

966 **OPEN RESEARCH**

967 TAMSAT data are publicly available to download at <https://www.tamsat.org.uk/>; please see
968 Maidment *et al.* (2014), Maidment *et al.* (2017) and Tarnavsky *et al.* (2014). The palaeobotanical
969 precipitation estimates compiled here are available as a spreadsheet, available to download at
970 Williams (2022). The DeepMIP PI and Eocene simulations are available by following the instructions
971 at <https://www.deepmip.org/data-eocene/>; please see Hollis *et al.* (2019).

972

973 **AUTHOR CONTRIBUTIONS**

974 CJRW carried out the analysis, produced the figures, wrote the manuscript and led the paper; all
975 authors contributed to writing subsequent drafts of the paper. DJL also carried out some of the
976 analysis, and provided guidance on the scientific discussion. WLC, AAO, YD, DKH, AMB, JBL,
977 PAM, IN, GK, SS, ZZ and JZ carried out the underlying DeepMIP model simulations. US, DRG,
978 GNI and TR collated and synthesised the proxy data. MH and BLOB provided guidance on the
979 scientific discussion and analysis.

980

981 **COMPETING INTERESTS**

982 The authors declare that they have no conflict of interest.

983

984 **ACKNOWLEDGEMENTS**

985 CJRW acknowledges the financial support of the UK Natural Environment Research Council funded
986 SWEET project (Super-Warm Early Eocene Temperatures), and that of the European Research
987 Council. WLC and AAO acknowledge funding from JSPS KAKENHI and MEXT KAKENHI, and
988 are grateful to JAMSTEC for use of the Earth Simulator. The numerical simulations performed by
989 DKH and AMB used resources provided by the Swedish National Infrastructure for Computing
990 (SNIC) at the National Supercomputer Centre (NSC), partially funded by the Swedish Research
991 Council. YD and JBL thank GENCI for providing access to the HPC resources of TGCC. PAM
992 thanks Evgeny Volodin and INM RAS for the help with INMCM simulations. GK acknowledges
993 financial support by PACES through the Helmholtz association and the computing centre of the
994 Alfred Wegener Institute in Bremerhaven and the DKRZ in Hamburg (Germany) for computational
995 resources, infrastructure and support. JZ and BLOB acknowledge support from the National Center
996 for Atmospheric Research, which is a major facility sponsored by the National Science Foundation.
997 US acknowledges funding from the Natural Environment Research Council. DRG acknowledges
998 funding from the Natural Sciences and Engineering Council of Canada. GNI acknowledges a GCRF
999 Royal Society Dorothy Hodgkin Fellowship.

1000

1001 **FINANCIAL SUPPORT**

1002 CJRW was supported by the UK Natural Environment Research Council-funded SWEET project
1003 (grant no. NE/P01903X/1) and that of the European Research Council under the European Union's
1004 Seventh Framework Programme (FP/2007-868 2013) (ERC grant agreement no. 340923 (TGRES)).
1005 WLC and AAO were supported by JSPS KAKENHI (grant no. 17H06104) and MEXT KAKENHI
1006 (grant no. 17H06323). AMB and DKH were partially funded by the Swedish Research Council
1007 through grant agreement no. 2016-03912 and 2020-04791, and DKH also acknowledges the support
1008 of FORMAS grant 2018-01621 and Australian Research Council grant DE220100279. The GFDL

1009 simulations were performed at NSC, partially funded by the Swedish Research Council through grant
1010 agreement no. 2018-05973. YD and JBL were supported by GENCI under allocation no. 2019-
1011 A0050102212. PAM was supported by the state assignment project no. AAAA-A19-119022190173-
1012 2 (FMGE-2019-0009). JZ and BLOB were supported by the National Science Foundation under
1013 cooperative agreement no. 1852977. US was supported by the Natural Environment Research
1014 Council (grant NE/P019137/1). DRG was supported by the Natural Sciences and Engineering
1015 Council of Canada (grant no. 2016-04337). GNI was supported by a GCRF Royal Society Dorothy
1016 Hodgkin Fellowship (DHF\R1\191178). MH acknowledges support from NSF OPP 1842059.

1017

1018

1019 **REFERENCES**

1020 Adeonipekun, P. A., Ehinola, O. A., Yussuph, I. A., Toluhi, A. and Oyelami, A.: Bio-sequence
1021 stratigraphy of Shagamu Quarry outcrop, Benin Basin, southwestern Nigeria, *World Applied Sciences*
1022 *Journal*, 18, 91-106, DOI: 10.5829/idosi.wasj.2012.18.01.3572, 2012.

1023
1024 Anagnostou, E., John, E. H., Babila, T. L., Sexton, P. F., Ridgwell, A., Lunt, D. J., Pearson, P. N.,
1025 Chalk, T. B., Pancost, R. D. and Foster, G. L.: Proxy evidence for state-dependence of climate
1026 sensitivity in the Eocene greenhouse, *Nature Communications*, 11(4436),
1027 <https://doi.org/10.1038/s41467-020-17887-x>, 2020.

1028
1029 Anagnostou, E., John, E. H., Edgar, K. M., Foster, G. L., Ridgwell, A., Inglis, G. N., Pancost, R. D.,
1030 Lunt D. J. and Pearson, P. N.: Changing atmospheric CO₂ concentration was the primary driver of
1031 early Cenozoic climate, *Nature*, 533, 380–384, <https://doi.org/10.1038/nature17423>, 2016.

1032
1033 Arakawa, A. and Schubert, W. H.: Interactions of cumulus cloud ensemble with the large-scale
1034 environment. Part I, *J. Atmos. Sci.*, 31, 671-701, [https://doi.org/10.1175/1520-](https://doi.org/10.1175/1520-0469(1974)031<0674:IOACCE>2.0.CO;2)
1035 [0469\(1974\)031<0674:IOACCE>2.0.CO;2](https://doi.org/10.1175/1520-0469(1974)031<0674:IOACCE>2.0.CO;2), 1974.

1036
1037 Arias, P. A., Bellouin, N., Coppola, E. et al.: Technical Summary. In *Climate Change 2021: The*
1038 *Physical Science Basis. Contribution of Working Group I to the Sixth Assessment Report of the*
1039 *Intergovernmental Panel on Climate Change* [Masson-Delmotte, V., Zhai, P., Pirani, A., Connors, S.
1040 L., Péan, C., Berger, S., Caud, N., Chen, Y., Goldfarb, L., Gomis, M. I., Huang, M., Leitzell, K.,
1041 Lonnoy, E., Matthews, J. B. R., Maycock, T. K., Waterfield, T., Yelekçi, O., Yu, R. and Zhou, B.
1042 (eds.)], Cambridge University Press, In Press, <https://www.ipcc.ch/report/ar6/wg1/#TS>, 2021.

1043
1044 Atta-Peters, D. and Salami, M. B.: Late Cretaceous to early Tertiary pollen grains from offshore Tano
1045 Basin, southwestern Ghana, *Revista Española de Micropaleontología*, 36(3), 451-465,
1046 <https://dialnet.unirioja.es/servlet/articulo?codigo=1070295>, 2004.

1047
1048 Ayugi, B., Zhihong, J., Zhu, H., Ngoma, H., Babaousmail, H., Rizwan, K. and Dike, V.: Comparison
1049 of CMIP6 and CMIP5 models in simulating mean and extreme precipitation over East Africa, *Int. J.*
1050 *Clim.*, <https://doi.org/10.1002/joc.7207>, 2021.

1051
1052 Beerling, D. J., Fox, A. and Anderson, C. W.: Quantitative uncertainty analyses of ancient
1053 atmospheric CO₂ estimates from fossil leaves, *AJS*, 309(9), 775-787, DOI:
1054 <https://doi.org/10.2475/09.2009.01>, 2009.

1055

1056 Bijl, P. K., Houben, A. J. P., Schouten, S., Bohaty, S. M., Sluijs, A., Reichart, G.-J., Sinninghe
1057 Damsté J. S. and Brinkhuis, H.: Transient middle Eocene atmospheric CO₂ and temperature
1058 variations, *Science*, 330(6005), 819-821, DOI: 10.1126/science.1193654, 2010.
1059

1060 Bony, S. and Emanuel, K. A.: A parameterization of the cloudiness associated with cumulus
1061 convection; evaluation using TOGA COARE data, *J. Atmos. Sci.*, 58(21), 3158-3183,
1062 [https://doi.org/10.1175/1520-0469\(2001\)058<3158:APOTCA>2.0.CO;2](https://doi.org/10.1175/1520-0469(2001)058<3158:APOTCA>2.0.CO;2), 2001.
1063

1064 Braconnot, P., Harrison, S. P., Otto-Bliesner, B. L., Abe-Ouchi, A., Jungclaus, J. and Peterchmitt, J.-
1065 Y.: The palaeoclimate modelling intercomparison project contribution to CMIP5, CLIVAR Exch.
1066 Newsl, 56, 15–19, 2011.
1067

1068 Braconnot, P., Otto-Bliesner, B., Harrison, S., Joussaume, S., Peterchmitt, J.-Y., Abe-Ouchi, A.,
1069 Crucifix, M., Driesschaert, E., Fichefet, Th., Hewitt, C. D., Kageyama, M., Kitoh, A., Laîné, A.,
1070 Loutre, M.-F., Marti, O., Merkel, U., Ramstein, G., Valdes, P., Weber, S. L., Yu, Y., and Zhao, Y.:
1071 Results of PMIP2 coupled simulations of the Mid-Holocene and Last Glacial Maximum – Part 1:
1072 experiments and large-scale features, *Clim. Past*, 3, 261-277, <https://doi.org/10.5194/cp-3-261-2007>,
1073 2007.
1074

1075 Bushell, A. C.: Chapter 2 Understanding the Unified Model (Section 2.1.1), in Matthews, D.: Unified
1076 Model User Guide, http://www.ukscience.org/_Media/UM_User_Guide.pdf, Accessed 22/9/21, 1998.
1077

1078 Cantrill, D. J., Bamford, M. K., Wagstaff, B. E. and Sauquet, H.: Early Eocene fossil plants from the
1079 Mwadui kimberlite pipe, Tanzania, *Review of Palaeobotany and Palynology*, 196, 19-35, DOI:
1080 10.1016/j.revpalbo.2013.04.002, 2013.
1081

1082 Carmichael, M. J., Lunt, D. J., Huber, M., Heinemann, M., Kiehl, J., LeGrande, A., Loftson, C. A.,
1083 Roberts, C. D., Sago, N., Shields, C., Valdes, P. J., Winguth, A., Winguth, C. and Pancost, R. D.: A
1084 model-model and data-data comparison for the early Eocene hydrological cycle, *Clim. Past*, 12, 455-
1085 481, doi:10.5194/cp-12-455-2016, 2016.
1086

1087 Carmichael, M. J., Pancost, R. D. and Lunt D. J.: Changes in the occurrence of extreme precipitation
1088 events at the Paleocene–Eocene thermal maximum, *Earth Planet. Sci. Lett.*, 501, 24-36,
1089 <https://doi.org/10.1016/j.epsl.2018.08.005>, 2018.
1090

1091 Chan, W.-L., Abe-Ouchi, A. and Ohgaito, R.: Simulating the mid- Pliocene climate with the MIROC
1092 general circulation model: experimental design and initial results, *Geosci. Model Dev.*, 4, 1035-1049,
1093 <https://doi.org/10.5194/gmd-4-1035-2011>, 2011.
1094
1095 Chiaghanam, O. I., Chiadikobi, K.C., Oguanya, C.E., Ikegwuonu, O.N., Nwokeabia, C.N.:
1096 Palynological and Paleoenvironmental Study of Paleogene in Bende - Umuahia, Niger Delta Basin,
1097 Nigeria, *Journal of Environment and Earth Science*, 7, 97-107, ISSN 2225-0948, 2017.
1098
1099 Cox, P. M.: A primitive equation, 3-dimensional model of the ocean, GFDL Ocean Group Technical
1100 Report No. 1, Geophysical Fluid Dynamics Laboratory, Princeton, New Jersey, 1984.
1101
1102 Cox, P. M., Betts, R. A., Bunton, C. B., Essery, R. L. H., Rowntree, P. R. & Smith, J.: The impact of
1103 new land surface physics on the GCM simulation of climate and climate sensitivity. *Clim. Dyn.*,
1104 15(3), 183-203. <https://doi.org/10.1007/s003820050276>, 1999.
1105
1106 Cramwinckel, M. J., Huber, M., Kocken, I. J., Agnini, C., Bijl, P. K., Bohaty, S. M., Frieling, J.,
1107 Goldner, A., Hilgen, F. J., Kip, E. L., Peterse, F., van der Ploeg, R., Röhl, U., Schouten, S. and Sluijs,
1108 A.: Synchronous tropical and polar temperature evolution in the Eocene, *nature* 559, 382–386,
1109 <https://doi.org/10.1038/s41586-018-0272-2>, 2018.
1110
1111 Crowley, C. W.: An atlas of Cenozoic climates, Masters of science in geology, The University of
1112 Texas, 2012.
1113
1114 de Villiers, S. E.: The palynology of Tertiary sediments from a palaeochannel in Namaqualand,
1115 Doctor of Philosophy thesis, Faculty of Science, University of Witwatersrand, Johannesburg, 100 pp.,
1116 1997.
1117
1118 Delworth, T. L., Broccoli, A. J., Rosati, A., Stouffer, R. J., Balaji, V., Beesley, J. A., Cooke, W. F.,
1119 Dixon, K.W., Dunne, J., Dunne, K. A., Durachta, J. W., Findell, K. L., Ginoux, P., Gnanadesikan, A.,
1120 Gordon, C. T., Griffies, S. M., Gudgel, R., Harrison, M. J., Held, I. M., Hemler, R. S., Horowitz, L.
1121 W., Klein, S. A., Knutson, T. R., Kushner, P. J., Langenhorst, A. R., Lee, H.-C., Lin, S.-J., Lu, J.,
1122 Malyshev, S. L., Milly, P. C. D., Ramaswamy, V., Russell, J., Schwarzkopf, M. D., Shevliakova, E.,
1123 Sirutis, J. J., Spelman, M. J., Stern, W. F., Winton, M., Wittenberg, A. T., Wyman, B., Zeng, F. and
1124 Zhang, R.: GFDL’s CM2 Global Coupled Climate Models. Part I: Formulation and Simulation
1125 Characteristics, *J. Climate*, 19, 643–674, <https://doi.org/10.1175/JCLI3629.1>, 2006.
1126

1127 Dufresne, J.-L., Foujols, M.-A., Denvil, S., Caubel, A., Marti, O., Aumont, O., Balkanski, Y., Bekki,
1128 S., Bellenger, H., Benshila, R., Bony, S., Bopp, L., Braconnot, P., Brockmann, P., Cadule, P., Cheruy,
1129 F., Codron, F., Cozic, A., Cugnet, D., de Noblet, N., Duvel, J.-P., Ethé, C., Fairhead, L., Fichet, T.,
1130 Flavoni, S., Friedlingstein, P., Grandpeix, J.-Y., Guez, L., Guilyardi, E., Hau all glustaine, D.,
1131 Hourdin, F., Idelkadi, A., Ghattas, J., Joussaume, S., Kageyama, M., Krinner, G., Labetoulle, S.,
1132 Lahellec, A., Lefebvre, M.-P., Lefevre, F., Levy, C., Li, Z. X., Lloyd, J., Lott, F., Madec, G., Mancip,
1133 M., Marchand, M., Masson, S., Meurdesoif, Y., Mignot, J., Musat, I., Parouty, S., Polcher, J., Rio, C.,
1134 Schulz, M., Swingedouw, D., Szopa, S., Talandier, C., Terray, P., Viovy, N. and Vuichard, N.:
1135 Climate Change Projections Using the IPSL-CM5 Earth System Model: From CMIP3 to CMIP5,
1136 *Clim. Dynam.*, 40, 2123-2165, <https://doi.org/10.1007/s00382-012-1636-1>, 2013.

1137

1138 Durre I., Menne, M. J., Gleason, B. E., Houston, T. G. and Vose, R. S.: Comprehensive automated
1139 quality assurance of daily surface observations, *J. Applied Meteor. and Climatol.*, 49, 1615-1633,
1140 [doi.10.1175/2010JAMC2375.1](https://doi.org/10.1175/2010JAMC2375.1), 2010.

1141

1142 Durre I., Menne, M. J. and Vose, R. S.: Strategies for evaluating quality assurance procedures, *J.*
1143 *Applied Meteor. and Climatol.*, 47, 1785-1791, [doi:10.1175/2007JAMC1706.1](https://doi.org/10.1175/2007JAMC1706.1), 2008.

1144

1145 Eaton, B.: User's Guide to the Community Atmosphere Model CAM-CAM-5.1.1, NCAR
1146 (https://www.cesm.ucar.edu/models/cesm1.0/cam/docs/ug5_1_1/ug.html), Accessed 10/9/21, 2010.

1147

1148 Edwards, J. M. and Slingo, A.: Studies with a flexible new radiation code. I: Choosing a configuration
1149 for a large-scale model. *Q.J.R. Meteorol. Soc.*, 122: 689-719. <https://doi.org/10.1002/qj.49712253107>,
1150 1996.

1151

1152 Eisawi, A. and Schrank, E.: Upper Cretaceous to Neogene palynology of the Melut Basin, southeast
1153 Sudan, *Palynology*, 32, 101-129, DOI: 10.1080/01916122.2008.9989653, 2008.

1154

1155 Emanuel, K. A.: A scheme for representing cumulus convection in large-scale models, *J. Atmos. Sci.*,
1156 48(21), 2313-2329, [https://doi.org/10.1175/1520-0469\(1991\)0482.0.CO;2](https://doi.org/10.1175/1520-0469(1991)0482.0.CO;2), 1991.

1157

1158 Eyring, V., Bony, S., Meehl, G. A., Senior, C. A., Stevens, B., Stouffer, R. J., and Taylor, K. E.:
1159 Overview of the Coupled Model Intercomparison Project Phase 6 (CMIP6) experimental design and
1160 organization, *Geosci. Model Dev.*, 9, 1937-1958, [doi:10.5194/gmd-9-1937-2016](https://doi.org/10.5194/gmd-9-1937-2016), 2016.

1161

1162 Farnsworth, A., Lunt, D. J., Robinson, S.A., Valdes, P.J., Roberts, W.H.G., Clift, P.D., Markwick, P.,
1163 Su, T., Wrobel, N., Bragg, F., Kelland, S.J. and Pancost, R.D.: Past East Asian monsoon evolution

1164 controlled by paleogeography, not CO₂. *Science Advances*, 5, 10, DOI: 10.1126/sciadv.aax1697,
1165 2019.

1166

1167 Fouquart, Y. and Bonnel, B.: Computations of solar heating of the Earth's atmosphere: A new
1168 parameterization, *Beitr. Phys. Atmos.*, 53, 35-62, 1980.

1169

1170 Funk, C., Nicholson, S., Landsfeld, M., Klotter, D., Peterson, P. and Harrison, L.: The Centennial
1171 Trends Greater Horn of Africa precipitation dataset, *Sci Data* 2, 150050,
1172 <https://doi.org/10.1038/sdata.2015.50>, 2015.

1173

1174 Galbraith, E. D., Kwon, E. Y., Gnanadesikan, A., Rodgers, K. B., Griffies, S. M., Bianchi, D.,
1175 Sarmiento, J. L., Dunne, J. P., Simeon, J., Slater, R. D., Wittenberg, A. T. and Held, I. M.: Climate
1176 Variability and Radiocarbon in the CM2Mc Earth System Model, *J. Clim.*, 24, 4230-4254,
1177 <https://doi.org/10.1175/2011JCLI3919.1>, 2011.

1178

1179 Gaskell, D. E., Huber, M., O'Brien, C. L., Inglis, G. N., Acosta, R. P., Poulsen, C. J. and Hull, P. M.:
1180 The latitudinal temperature gradient and its climate dependence as inferred from foraminiferal $\delta^{18}O$
1181 over the past 95 million years, *PNAS*, 119 (11), <https://doi.org/10.1073/pnas.2111332119>, 2022.

1182

1183 Goha, R. B., Zeli, B. D., Konan, R. Y., Tea-Yassi, J., Kouadio, D. K. and Tahi, I.: Stratigraphie
1184 palynologique du Maastrichtien supérieur-Eocène supérieur du bassin sédimentaire offshore de Côte
1185 d'Ivoire, Afrique de l'ouest, *International Journal of African Studies*, 6, 40-57, 2016.

1186

1187 Grant, A.: Chapter 2 Understanding the Unified Model (Section 2.1.6), in Matthews, D.: *Unified*
1188 *Model User Guide*, http://www.ukscience.org/_Media/UM_User_Guide.pdf, Accessed 22/9/21, 1998.

1189

1190 Guo, C., Bentsen, M., Bethke, I., Ilicak, M., Tjiputra, J., Toniazzo, T., Schwinger, J. and Otterå, O.
1191 H.: Description and evaluation of NorESM1_F: a fast version of the Norwegian Earth System Model
1192 (NorESM), *Geosci. Model Dev.*, 12, 343-362, <https://doi.org/10.5194/gmd-12-343-2019>, 2019.

1193

1194 Hack, J. J.: Parameterization of moist convection in the NCAR Community Climate Model CCM2, *J.*
1195 *Geophys. Res. Atmos.*, 99(D3): 5551-5568, DOI:10.1029/93JD03478, 1994.

1196

1197 Hagemann, S.: An improved land surface parameter dataset for global and regional climate models,
1198 Max Planck Institute for Meteorology, Report No. 336,
1199 <https://citeseerx.ist.psu.edu/viewdoc/download?doi=10.1.1.471.2882&rep=rep1&type=pdf>, Accessed
1200 17/9/21, 2002.

1201
1202 Harrison, S. P. and Prentice, I. C.: Climate and CO₂ controls on global vegetation distribution at the
1203 last glacial maximum: analysis based on palaeovegetation data, biome modelling and palaeoclimate
1204 simulations, *Glob. Change Bio.*, 9 (7), 983-1004, <https://doi.org/10.1046/j.1365-2486.2003.00640.x>,
1205 2003.
1206
1207 Harrison, S. P., Bartlein, P. J., Brewer, S., Prentice, I. C., Boyd, M., Hessler, I., Holmgren, K., Izumi,
1208 K. and Willis, K.: Climate model benchmarking with glacial and mid-Holocene climates, *Clim. Dyn.*,
1209 43, 671-688, <https://doi.org/10.1007/s00382-013-1922-6>, 2014.
1210
1211 Hasumi, H.: CCSR Ocean Component Model (COCO) Version 2.1, Technical Report, The University
1212 of Tokyo, Tokyo, Japan, 2000.
1213
1214 Haywood, A. M., Tindall, J. C., Dowsett, H. J., Dolan, A. M., Foley, K. M., Hunter, S. J., Hill, D. J.,
1215 Chan, W.-L., Abe-Ouchi, A., Stepanek, C., Lohmann, G., Chandan, D., Peltier, W. R., Tan, N.,
1216 Contoux, C., Ramstein, G., Li, X., Zhang, Z., Guo, C., Nisancioglu, K. H., Zhang, Q., Li, Q., Kamae,
1217 Y., Chandler, M. A., Sohl, L. E., Otto-Bliesner, B. L., Feng, R., Brady, E. C., von der Heydt, A. S.,
1218 Baatsen, M. L. J. and Lunt, D. J.: The Pliocene Model Intercomparison Project Phase 2: large-scale
1219 climate features and climate sensitivity, *Clim. Past*, 16, 2095-2123, [https://doi.org/10.5194/cp-16-](https://doi.org/10.5194/cp-16-2095-2020)
1220 2095-2020, 2020.
1221
1222 Held, I. M. and Soden, B. J.: Robust Responses of the Hydrological Cycle to Global Warming, *J.*
1223 *Clim.*, 19 (21), 5686-5699, DOI: <https://doi.org/10.1175/JCLI3990.1>, 2006.
1224
1225 Herold, N., Buzan, J., Seton, M., Goldner, A., Green, J. A. M., Müller, R. D., Markwick, P. and
1226 Huber, M.: A suite of early Eocene (~55 Ma) climate model boundary conditions, *Geosci. Model*
1227 *Dev.*, 7, 2077-2090, doi:10.5194/gmd-7-2077-2014, 2014.
1228
1229 Hijmans, R. J., Cameron, S. E., Parra, J. L., Jones, P. G. and Jarvis, A.: Very high resolution
1230 interpolated climate surfaces for global land areas, *Int. J. Clim.*, 25, 1965-1978,
1231 <https://doi.org/10.1002/joc.1278>, 2005.
1232
1233 Huber, M. and Caballero, R.: The early Eocene equable climate problem revisited, *Clim. Past*, 7, 603-
1234 633, doi:10.5194/cp-7-603-2011, 2011.
1235
1236 Hurrell, J. W., Holland, M. M., Gent, P. R., Ghan, S., Kay, J. E., Kushner, P. J., Lamarque, J. F.,
1237 Large, W. G., Lawrence, D., Lindsay, K., Lipscomb, W. H., Long, M. C., Mahowald, N., Marsh, D.

1238 R., Neale, R. B., Rasch, P., Vavrus, S., Vertenstein, M., Bader, D., Collins, W. D., Hack, J. J., Kiehl,
1239 J. T. and Marshall, S.: The community earth system model: A framework for collaborative research,
1240 B. Am. Meteorol. Soc., 94, 1339-1360, <https://doi.org/10.1175/BAMS-D-12-00121.1>, 2013.
1241
1242 Hutchinson, D. K., de Boer, A. M., Coxall, H. K., Caballero, R., Nilsson, J. and Baatsen, M.: Climate
1243 sensitivity and meridional overturning circulation in the late Eocene using GFDL CM2.1, *Clim. Past*,
1244 14, 789-810, <https://doi.org/10.5194/cp-14-789-2018>, 2018.
1245
1246 Hollis, C. J., Dunkley Jones, T., Anagnostou, E., Bijl, P. K., Cramwinckel, M. J., Cui, Y., Dickens, G.
1247 R., Edgar, K. M., Eley, Y., Evans, D., Foster, G. L., Frieling, J., Inglis, G. N., Kennedy, E. M.,
1248 Kozdon, R., Lauretano, V., Lear, C. H., Littler, K., Lourens, L., Meckler, A. N., Naafs, B. D. A.,
1249 Pälike, H., Pancost, R. D., Pearson, P. N., Röhl, U., Royer, D. L., Salzmann, U., Schubert, B. A.,
1250 Seebeck, H., Sluijs, A., Speijer, R. P., Stassen, P., Tierney, J., Tripathi, A., Wade, B., Westerhold, T.,
1251 Witkowski, C., Zachos, J. C., Zhang, Y. G., Huber, H. and Lunt, D. J.: The DeepMIP contribution to
1252 PMIP4: methodologies for selection, compilation and analysis of latest Paleocene and early Eocene
1253 climate proxy data, incorporating version 0.1 of the DeepMIP database, *Geosci. Model Dev.*, 12,
1254 3149–3206, <https://doi.org/10.5194/gmd-12-3149-2019>, 2019.
1255
1256 Holtslag, A. and Boville, B.: Local versus nonlocal boundary-layer diffusion in a global climate
1257 model, *J. Clim.*, 6, 1825-1825, [https://doi.org/10.1175/1520-](https://doi.org/10.1175/1520-0442(1993)006<1825:LVNBLD>2.0.CO;2)
1258 [0442\(1993\)006<1825:LVNBLD>2.0.CO;2](https://doi.org/10.1175/1520-0442(1993)006<1825:LVNBLD>2.0.CO;2), 1993.
1259
1260 Hyland, E., Sheldon, N. D. and Fan, M.: Terrestrial paleoenvironmental reconstructions indicate
1261 transient peak warming during the early Eocene climatic optimum, *Geol. Soc. Am. Bull.*, 125(7-8),
1262 1338-1348, DOI:10.1130/B30761.1, 2013.
1263
1264 Inglis, G. N., Bragg, F., Burls, N. J., Cramwinckel, M. J., Evans, D., Foster, G. L., Huber, M., Lunt,
1265 D. J., Siler, N., Steinig, S., Tierney, J. E., Wilkinson, R., Anagnostou, E., de Boer, A. M., Dunkley
1266 Jones, T., Edgar, K. M., Hollis, C. J., Hutchinson, D. K., and Pancost, R. D.: Global mean surface
1267 temperature and climate sensitivity of the early Eocene Climatic Optimum (EECO), Paleocene–
1268 Eocene Thermal Maximum (PETM), and latest Paleocene, *Clim. Past*, 16, 1953-1968,
1269 <https://doi.org/10.5194/cp-16-1953-2020>, 2020.
1270
1271 IPCC: Climate Change 2013: The Physical Science Basis. Contribution of Working Group I to the
1272 Fifth Assessment Report of the Intergovernmental Panel on Climate Change [Stocker, T. F., D. Qin,
1273 G.-K. Plattner, M. Tignor, S. K. Allen, J. Boschung, A. Nauels, Y. Xia, V. Bex and P. M. Midgley

1274 (eds.]), Cambridge University Press, Cambridge, United Kingdom and New York, NY, USA, pp
1275 1535, <https://www.ipcc.ch/report/ar5/wg1/>, 2013.

1276

1277 IPCC: Climate Change 2021: The Physical Science Basis. Contribution of Working Group I to the
1278 Sixth Assessment Report of the Intergovernmental Panel on Climate Change [Masson-Delmotte, V.,
1279 P. Zhai, A. Pirani, S.L. et al. (eds.)], Cambridge University Press, Cambridge, United Kingdom,
1280 <https://www.ipcc.ch/report/ar6/wg1/>, 2021.

1281

1282 Jacobs, B. F. and Herendeen, P. S.: Eocene dry climate and woodland vegetation in tropical Africa
1283 reconstructed from fossil leaves from northern Tanzania, *Palaeogeography, Palaeoclimatology,*
1284 *Palaeoecology*, 213, 115-123, 10.1016/S0031-0182(04)00368-2, 2004.

1285

1286 Jungclaus, J. H., Keenlyside, N., Botzet, M., Haak, H., Luo, J.-J., Latif, M., Marotzke, J.,
1287 Mikolajewicz, U. and Roeckner, E.: Ocean circulation and tropical variability in the coupled model
1288 ECHAM5/MPI-OM, *J. Climate*, 19, 3952-3972, <https://doi.org/10.1175/JCLI3827.1>, 2006.

1289

1290 K-1 model developers: K-1 coupled model (MIROC) description, Technical Report, Center for
1291 Climate System Research (University of Tokyo), National Institute for Environmental Studies,
1292 Frontier Research Center for Global Change, Tokyo, Japan, 2004.

1293

1294 Kageyama, M., Braconnot, P., Harrison, S. P., Haywood, A. M., Jungclaus, J. H., Otto-Bliesner, B. L.,
1295 Peterschmitt, J.-Y., Abe-Ouchi, A., Albani, S., Bartlein, P. J., Brierley, C., Crucifix, M., Dolan, A.,
1296 Fernandez-Donado, L., Fischer, H., Hopcroft, P. O., Ivanovic, R. F., Lambert, F., Lunt, D. J.,
1297 Mahowald, N. M., Peltier, W. R., Phipps, S. J., Roche, D. M., Schmidt, G. A., Tarasov, L., Valdes, P.
1298 J., Zhang, Q. and Zhou, T.: The PMIP4 contribution to CMIP6 – Part 1: Overview and over-arching
1299 analysis plan, *Geosci. Model Dev.*, 11, 1033–1057, <https://doi.org/10.5194/gmd-11-1033-2018>, 2018.

1300

1301 Kaiser, T. M. Ansorge, J., Arratia, G., Bullwinkel, V., Gunnell, G. F., Herendeen, P. S., Jacobs, B.,
1302 Mingram, J., Msuya, C., Musolff, A., Naumann, R., Schulz, E. and Wilde, V.: The maar lake of
1303 Mahenge (Tanzania) unique evidence of Eocene terrestrial environments in sub-Saharan Africa,
1304 *Zeitschrift der Deutschen Gesellschaft für Geowissenschaften Band 157 Heft 3*, DOI: 10.1127/1860-
1305 1804/2006/0157-0411, 2006.

1306

1307 Kaplan, J. O., Bigelow, N. H., Prentice, I. C., Harrison, S. P., Bartlein, P. J., Christensen, T. R.,
1308 Cramer, W., Matveyeva, N. V., McGuire, A. D., Murray, D. F., Razzhivin, V. Y., Smith, B., Walker,
1309 D. A., Anderson, P. M., Andreev, A. A., Brubaker, L. B., Edwards, M. E. and Lozhkin, A. V.:

1310 Climate change and Arctic ecosystems: 2. Modeling, paleodata-model comparisons, and future
1311 projections, *J. Geophys. Res.*, 108, 8171, doi:10.1029/2002jd002559, 2003.
1312
1313 Keery, J. S., Holden, P. B. and Edwards, N. R.: Sensitivity of the Eocene climate to CO₂ and orbital
1314 variability, *Clim. Past*, 14, 215-238, DOI: 10.5194/cp-14-215-2018, 2018
1315
1316 Kennedy-Asser, A. T., Lunt, D. J., Farnsworth, A. and Valdes, P. J.: Assessing mechanisms and
1317 uncertainty in modeled climatic change at the Eocene-Oligocene transition, *Paleoceanography and*
1318 *Paleoclimatology*, 34, 16-34. <https://doi.org/10.1029/2018PA003380>, 2019.
1319
1320 Laval, K., Sadourny, R. and Serafini, Y.: Land surface processes in a simplified general circulation
1321 model, *Geophys. Astrophys. Fluid Dyn.*, 17(1), 129-150,
1322 <https://doi.org/10.1080/03091928108243677>, 1981.
1323
1324 Li, X., Guo, C., Zhang, Z., Otterå, O. H. and Zhang, R.: PlioMIP2 simulations with NorESM-L and
1325 NorESM1-F, *Clim. Past*, 16, 183-197, <https://doi.org/10.5194/cp-16-183-2020>, 2020.
1326
1327 Licht, A., van Cappelle, M., Abels, H. Ladant, J.-B., Trabucho-Alexandre, J., France-Lanord, C.,
1328 Donnadieu, Y., Vandenberghe, J., Rigaudier, T., Lécuyer, C., Terry Jr, D., Adriaens, R., Boura, A.,
1329 Guo, Z., Naing Soe, A., Quade, J., Dupont-Nivet, G. and Jaeger, J.-J.: Asian monsoons in a late
1330 Eocene greenhouse world, *Nature*, 513, 501–506, <https://doi.org/10.1038/nature13704>, 2014.
1331
1332 Liebmann, B., Bladé, I., Kiladis, G. N., Carvalho, L. M. V., Senay, G. B., Allured, D., Leroux, S. and
1333 Funk, C.: Seasonality of African Precipitation from 1996 to 2009, *J. Clim.*, 25 (12), 4304-4322, DOI:
1334 <https://doi.org/10.1175/JCLI-D-11-00157.1>, 2012.
1335
1336 Liu, W., Xie, S.-P., Liu, Z. and Zhu, J.: Overlooked possibility of a collapsed Atlantic Meridional
1337 Overturning Circulation in warming climate, *Science Advances*, 3(1), e1601666.
1338 <https://doi.org/10.1126/sciadv.1601666>, 2017.
1339
1340 Liu, X. D., Dong, B. W., Yin, Z. Y., Smith, R. S. and Guo, Q. C.: Continental drift, plateau uplift, and
1341 the evolutions of monsoon and arid regions in Asia, Africa, and Australia during the Cenozoic,
1342 *Science China-Earth Sciences*, 62, 1053-1075, DOI: 10.1007/s11430-018-9337-8, 2019.
1343
1344 Loftson, C. A., Lunt, D. J. And Francis, J. E.: Investigating vegetation-climate feedbacks during the
1345 early Eocene, *Clim. Past*, 10, 419-436, doi:10.5194/cp-10-419-2014, 2014.
1346

1347 Lott, F.: Alleviation of stationary biases in a GCM through a mountain drag parameterization scheme
1348 and a simple representation of mountain lift forces, *Mon. Wea. Rev.*, 127(5), 788-801,
1349 [https://doi.org/10.1175/1520-0493\(1999\)127<0788:AOSBIA>2.0.CO;2](https://doi.org/10.1175/1520-0493(1999)127<0788:AOSBIA>2.0.CO;2), 1999.
1350

1351 Louis, J. F.: A parametric model of vertical eddy fluxes in the atmosphere, *Boundary-Layer*
1352 *Meteorol.*, 17(2), 187-202, <https://doi.org/10.1007/BF00117978>, 1979.
1353

1354 Lunt, D. J., Bragg, F., Chan, W.-L., Hutchinson, D. K., Ladant, J.-B., Morozova, P., Niezgodzki, I.,
1355 Steinig, S., Zhang, Z., Zhu, J., Abe-Ouchi, A., Anagnostou, E., de Boer, A. M., Coxall, H. K.,
1356 Donnadieu, Y., Foster, G., Inglis, G. N., Knorr, G., Langebroek, P. M., Lear, C. H., Lohmann, G.,
1357 Poulsen, C. J., Sepulchre, P., Tierney, J. E., Valdes, P. J., Volodin, E. M., Dunkley Jones, T., Hollis,
1358 C. J., Huber, M. and Otto-Bliesner, B. L.: DeepMIP: model intercomparison of early Eocene climatic
1359 optimum (EECO) large-scale climate features and comparison with proxy data, *Clim. Past*, 17, 203-
1360 227, <https://doi.org/10.5194/cp-17-203-2021>, 2021.
1361

1362 Lunt, D. J., Dunkley Jones, T., Heinemann, M., Huber, M., LeGrande, A., Winguth, A., Loftson, C.,
1363 Marotzke, J., Roberts, C. D., Tindall, J., Valdes, P. and Winguth, C.: A model-data comparison for a
1364 multi-model ensemble of early Eocene atmosphere-ocean simulations: EoMIP, *Clim. Past*, 8, 1717-
1365 1736, <https://doi.org/10.5194/cp-8-1717-2012>, 2012.
1366

1367 Lunt, D. J., Huber, M., Anagnostou, E., Baatsen, M. L. J., Caballero, R., DeConto, R., Dijkstra, H. A.,
1368 Donnadieu, Y., Evans, D., Feng, R., Foster, G. L., Gasson, E., von der Heydt, A. S., Hollis, C. J.,
1369 Inglis, G. N., Jones, S. M., Kiehl, J., Kirtland Turner, S., Korty, R. L., Kozdon, R., Krishnan, S.,
1370 Ladant, J.-B., Langebroek, P., Lear, C. H., LeGrande, A. N., Littler, K., Markwick, P., Otto-Bliesner,
1371 B., Pearson, P., Poulsen, C. J., Salzmann, U., Shields, C., Snell, K., Stärz, M., Super, J., Tabor, C.,
1372 Tierney, J. E., Tourte, G. J. L., Tripathi, A., Upchurch, G. R., Wade, B. S., Wing, S. L., Winguth, A.
1373 M. E., Wright, N. M., Zachos, J. C. and Zeebe, R. E.: The DeepMIP contribution to PMIP4:
1374 experimental design for model simulations of the EECO, PETM, and pre-PETM (version 1.0),
1375 *Geosci. Model Dev.*, 10, 889-901, <https://doi.org/10.5194/gmd-10-889-2017>, 2017.
1376

1377 Ma, Y. Q., Fan, M. J., Lu, Y. C., Liu, H. M., Zhang, S. P. and Liu, X. F.: Stable isotope record of
1378 middle Eocene summer monsoon and its instability in eastern China, *Global and Planetary Change*,
1379 175, 103-112, DOI: 10.1016/j.gloplacha.2019.02.007, 2019.
1380

1381 Maidment, R. I., Grimes, D., Black, E., Tarnavsky, E., Young, M., Greatrex, H., Allan, R. P., Stein,
1382 T., Nkonde, E., Senkunda, S. and Alcántara, E. M. U.: A new, long-term daily satellite-based rainfall

1383 dataset for operational monitoring in Africa, *nature Scientific Data*, 4: 170063. DOI:
1384 10.1038/sdata.2017.63, 2017.

1385

1386 Maidment, R. I., Grimes, D., Allan, R. P., Tarnavsky, E., Stringer, M., Hewison, T., Roebeling, R.
1387 and Black, E.: The 30-year TAMSAT African Rainfall Climatology and Time-series (TARCAT) Data
1388 Set, *J. Geophys. Res.: Atmos.*, 119(10): 619-610, 644. DOI: 10.1002/2014JD021927, 2014.

1389

1390 Marsland, S. J., Haak, H., Jungclaus, J. H., Latif, M. and Roske, F.: The Max-Planck-Institute global
1391 ocean/sea ice model with orthogonal curvilinear coordinates, *Ocean Model.*, 5, 91-127,
1392 [https://doi.org/10.1016/S1463-5003\(02\)00015-X](https://doi.org/10.1016/S1463-5003(02)00015-X), 2003.

1393

1394 Martínez-Botí, M. A., Foster, G. L., Chalk, T. B., Rohling, E. J., Sexton, P. F., Lunt, D. J., Pancost, R.
1395 D., Badger, M. P. S. and Schmidt, D. N.: Plio-Pleistocene climate sensitivity evaluated using high-
1396 resolution CO₂ records, *Nature*, 518, 49-54, <https://doi.org/10.1038/nature14145>, 2015.

1397

1398 Menne, M. J., Durre I., Vose, R. S., Gleason, B. E. and Houston, T. G.: An overview of the Global
1399 Historical Climatology Network-Daily Database, *J. Atmos. and Oceanic Tech.*, 29, 897-910,
1400 [doi.10.1175/JTECH-D-11-00103.1](https://doi.org/10.1175/JTECH-D-11-00103.1), 2012.

1401

1402 Monerie, P-A., Wainwright, C. M. and Sidibe, M.: Model uncertainties in climate change impacts on
1403 Sahel precipitation in ensembles of CMIP5 and CMIP6 simulations, *Clim. Dyn.*, 55, 1385-1401,
1404 <https://doi.org/10.1007/s00382-020-05332-0>, 2020.

1405

1406 Moorthi, S. and Suarez, M. J.: Relaxed Arakawa-Schubert. A Parameterization of Moist Convection
1407 for General Circulation Models, *Mon. Weather Rev.*, 120, 978-1002, [https://doi.org/10.1175/1520-0493\(1992\)120<0978:RASAPO>2.0.CO;2](https://doi.org/10.1175/1520-0493(1992)120<0978:RASAPO>2.0.CO;2), 1992.

1408

1409

1410 Morcrette, J. J., Smith, L. and Fouquart, Y.: Pressure and temperature dependence of the absorption
1411 in longwave radiation parameterizations, *Beitr. Phys. Atmos.*, 59, 455-469, ISSN 0005-8173, 1986.

1412

1413 Morley, R. J.: Cretaceous and Tertiary climate change and the past distribution of megathermal
1414 rainforests, in: *Tropical Rainforest Responses to Climatic Change*, Springer Praxis Books, Springer
1415 Berlin Heidelberg, 1–31, 2007.

1416

1417 Morrison, H. and Gettelman, A.: A New Two-Moment Bulk Stratiform Cloud Microphysics Scheme
1418 in the Community Atmosphere Model, Version 3 (CAM3). Part I: Description and Numerical Tests, *J.*
1419 *Clim.*, 21(15), 3642-3659, DOI:10.1175/2008JCLI2105.1, 2008.

1420
1421 Naafs, B. D. A., Rohrssen, M., Inglis, G. N., Lähteenoja, O., Feakins, S. J., Collinson, M. E.,
1422 Kennedy, E. M., Singh, P. K., Singh, M. P., Lunt, D. J. and Pancost, R. D.: High temperatures in the
1423 terrestrial mid-latitudes during the early Palaeogene, *Nature Geosci* 11, 766-771,
1424 <https://doi.org/10.1038/s41561-018-0199-0>, 2018.
1425
1426 Neale, R. B., Richter, J. H. and Jochum M.: The impact of convection on ENSO: From a delayed
1427 oscillator to a series of events, *J. Clim.*, 21(22), 5904-5924, <https://doi.org/10.1175/2008JCLI2244.1>,
1428 2008.
1429
1430 Neale, R. B., Richter, J. H., Park, S., Lauritzen, P. H., Vavrus, S. J., Rasch, P. J. and Zhang, M.: The
1431 Mean Climate of the Community Atmosphere Model (CAM4) in Forced SST and Fully Coupled
1432 Experiments, *J. Clim.*, 26(14), 5150-5168, <https://doi.org/10.1175/JCLI-D-12-00236.1>, 2013.
1433
1434 Okeke, K. K. and Umeji, O. P.: Palynostratigraphy, palynofacies and palaeoenvironment of deposition
1435 of Selandian to Aquitanian sediments, southeastern Nigeria, *Journal of African Earth Sciences*, 120,
1436 102-124, DOI: 10.1016/j.jafrearsci.2016.04.020, 2016
1437
1438 Park, S. and Bretherton, C. S.: The University of Washington Shallow Convection and Moist
1439 Turbulence Schemes and Their Impact on Climate Simulations with the Community Atmosphere
1440 Model, *J. Clim.*, 22(12), 3449-3469, DOI:10.1175/2008JCLI2557.1, 2009.
1441
1442 Pearson, P. N. and Wade, B. S.: Stable warm tropical climate through the Eocene Epoch, *Geology*, 35
1443 (1), <https://doi.org/10.1130/G24462Y.1>, 2007.
1444
1445 Quan, C., Liu, Y. S. and Utescher, T.: Eocene monsoon prevalence over China: A paleobotanical
1446 perspective, *Palaeogeography Palaeoclimatology Palaeoecology*, 365, 302-311, DOI:
1447 10.1016/j.palaeo.2012.09.035, 2012.
1448
1449 Rae, J. W. B., Zhang, Y. G., Liu, X., Foster, G. L., Stoll, H. M. and Whiteford, R. D. M.: Atmospheric
1450 CO₂ over the past 66 million years from marine archives, *Annual Review of Earth and Planetary*
1451 *Sciences*, 49, 606-641, <https://doi.org/10.1146/annurev-earth-082420-063026>, 2021.
1452
1453 Rasch, P. J. and Kristjánsson, J. E.: A comparison of the CCM3 model climate using diagnosed and
1454 predicted condensate parameterizations, *J. Clim.*, 11(7), 1587-1614, [https://doi.org/10.1175/1520-0442\(1998\)011<1587:ACOTCM>2.0.CO;2](https://doi.org/10.1175/1520-0442(1998)011<1587:ACOTCM>2.0.CO;2), 1998.
1455
1456

1457 Reichgelt, T., D'Andrea, W. J. and Fox, B. R. S.: Abrupt plant physiological changes in southern New
1458 Zealand at the termination of the Mi-1 event reflect shifts in hydroclimate and pCO₂, *EPSL*, 455, 115–
1459 124, <https://doi.org/10.1016/j.epsl.2016.09.026>, 2016.
1460

1461 Reichgelt, T., Greenwood, D. R., Steinig, S., Conran, J. G., Hutchinson, D. K., Lunt, D. J., Scriven, L.
1462 J., and Zhu, J.: Plant proxy evidence for high rainfall and productivity in the Eocene of Australia,
1463 *Paleoceanography and Paleoclimatology*, <https://doi.org/10.1029/2022PA004418>, 2022.
1464

1465 Richter, J. H. and Rasch, P. J.: Effects of convective momentum transport on the atmospheric
1466 circulation in the Community Atmosphere Model, version 3, *J. Clim.*, 21, 1487-1499,
1467 <https://doi.org/10.1175/2007JCLI1789.1>, 2008.
1468

1469 Roeckner, E., Bäuml, G., Bonaventura, L., Brokopf, R., Esch, M., Giorgetta, M., Hagemann, S.,
1470 Kirchner, I., Kornbleuh, L., Manzini, E., Rhodin, A., Schlese, U., Schulzweida, U. and Tompkins, A.:
1471 The atmospheric general circulation model ECHAM 5. PART I: Model description, Report 349, Max-
1472 Planck Institut für Meteorologie, Hamburg, Germany, 140 pp., 2003.
1473

1474 Rotstajn, L. D.: A physically based scheme for the treatment of stratiform clouds and precipitation in
1475 large-scale models. I: Description and evaluation of the microphysical processes, *Q. J. R. Meteorol.*
1476 *Soc.*, 123, 1227–1282, <https://doi.org/https://doi.org/10.1002/qj.49712354106>, 1997.
1477

1478 Rougier, J. C., Goldstein, M. and House, L.: Second-order exchangeability analysis for multi-model
1479 ensembles, *Journal of the American Statistical Association*, 108, 852-863,
1480 [doi:10.1080/01621459.2013.802963](https://doi.org/10.1080/01621459.2013.802963), 2013.
1481

1482 Salami, M. B.: Late Cretaceous and Early Tertiary Palynofacies of Southwestern Nigeria, *Revista*
1483 *Espanola de Micropaleontologia*, XVI, 415-423, 1984.
1484

1485 Salard-Chebouldaëff, M.: Palynologie Maestrichtienne et Tertiaire du Cameroun. Etude qualitative et
1486 repartition verticale des principales especes, *Review of Palaeobotany and Palynology*, 28, 365-388,
1487 [https://doi.org/10.1016/0034-6667\(79\)90032-0](https://doi.org/10.1016/0034-6667(79)90032-0), 1979.
1488

1489 Salerno, J., Diem, J. E., Konecky, B. L. and Hartter, J.: Recent intensification of the seasonal rainfall
1490 3391 cycle in equatorial Africa revealed by farmer perceptions, satellite-based estimates, and ground-
1491 based station 3392 measurements, *Climatic Change*, 153(1-2):123-139, DOI:10.1007/s10584-019-
1492 02370-4, 2019.
1493

1494 Sepulchre, P., Caubel, A., Ladant, J.-B., Bopp, L., Boucher, O., Braconnot, P., Brockmann, P., Cozic,
1495 A., Donnadiou, Y., Dufresne, J.-L., Estella-Perez, V., Ethé, C., Fluteau, F., Foujols, M.-A., Gastineau,
1496 G., Ghattas, J., Hauglustaine, D., Hourdin, F., Kageyama, M., Khodri, M., Marti, O., Meurdesoif, Y.,
1497 Mignot, J., Sarr, A.-C., Servonnat, J., Swingedouw, D., Szopa, S. and Tardif, D.: IPSL-CM5A2 – an
1498 Earth system model designed for multi-millennial climate simulations, *Geosci. Model Dev.*, 13, 3011-
1499 3053, <https://doi.org/10.5194/gmd-13-3011-2020>, 2020.

1500

1501 Smagorinsky, J.: General Circulation Experiments with the Primitive Equations: I The Basic
1502 Experiment, *Mon. Weather Rev.*, 91, 99-164, [https://doi.org/10.1175/1520-
1503 0493\(1963\)091<0099:GCEWTP>2.3.CO;2](https://doi.org/10.1175/1520-0493(1963)091<0099:GCEWTP>2.3.CO;2), 1963.

1504

1505 Stepanek, C. and Lohmann, G.: Modelling mid-Pliocene climate with COSMOS, *Geosci. Model Dev.*,
1506 5, 1221-1243, <https://doi.org/10.5194/gmd-5-1221-2012>, 2012.

1507

1508 Takata, K., Watanabe, T. and Emori, S.: Development of the minimal advanced treatments of surface
1509 interaction and runoff, *Global Planet. Change*, 38, 209-222, doi:10.1016/S0921-8181(03)00030-4,
1510 2003.

1511

1512 Tarnavsky, E., Grimes, D., Maidment, R. I., Black, E., Allan, R. P., Stringer, M., Chadwick, R. and
1513 Kayitakire, F.: Extension of the TAMSAT Satellite-based Rainfall Monitoring over Africa and from
1514 1983 to present. *J. Applied Meteor. and Climatol.*, 53(12): 2805-2822. DOI: 10.1175/JAMC-D-14-
1515 0016.1, 2014.

1516

1517 Taylor, K. E., Stouffer, R. J. and Meehl, G. A.: An overview of CMIP5 and the experiment design, *B.*
1518 *Am. Meteorol. Soc.*, 93, 485-498, <https://doi.org/10.1175/BAMS-D-11-00094.1>, 2011.

1519

1520 Tiedtke, M.: Representation of Clouds in Large-Scale Models, *Mon. Weather Rev.*, 121, 3040-3061,
1521 [https://doi.org/10.1175/1520-0493\(1993\)121<3040:ROCILS>2.0.CO;2](https://doi.org/10.1175/1520-0493(1993)121<3040:ROCILS>2.0.CO;2), 1993.

1522

1523 Tierney, J. E., Poulsen, C. J., Montañez, I. P., Bhattacharya, T., Feng, R., Ford, H. L., Hönlisch, B.,
1524 Inglis, G. N., Petersen, S. V., Sahoo, N., Tabor, C. R., Thirumalai, K., Zhu, J., Burls, N. J., Foster, G.
1525 L., Goddérís, Y., Huber, B. T., Ivany, L. C., Turner, S. K., Lunt, D. J., McElwain, J. C., Mills, B. J.
1526 W., Otto-Bliesner, B. L., Ridgwell, A. and Zhang, Y.-G.: Past climates inform our future, *Science*,
1527 370 (6510), DOI: 10.1126/science.aay3701, 2020.

1528

1529 Tokioka, T., Yamazaki, K., Kitoh, A. and Ose, T.: The Equatorial 30-60 day Oscillation and the
1530 Arakawa-Schubert Penetrative Cumulus Parameterization, *J. Meteorol. Soc. Japan*, 66, 883-901,
1531 https://doi.org/10.2151/jmsj1965.66.6_883, 1988.

1532

1533 Utescher, T., Bruch, A. A., Erdei, B., François, L., Ivanov, D., Jacques, F. M. B., Kern, A. K., Liu,
1534 Y.-S., Mosbrugger, V. and Spicer, R. A.: The Coexistence Approach - Theoretical background and
1535 practical considerations of using plant fossils for climate quantification, *Palaeogeography,*
1536 *Palaeoclimatology, Palaeoecology*, 410, 58-73, <https://doi.org/10.1016/j.palaeo.2014.05.031>, 2014.

1537

1538 Utescher, T. and Mosbrugger, V.: Eocene vegetation patterns reconstructed from plant diversity – A
1539 global perspective, *Palaeogeogr. Palaeoclimatol.*, 247, 243–271, doi:10.1016/j.palaeo.2006.10.022, 2007.

1540

1541 Uzodimma, D. E.: Palynostratigraphy, Age Determination and Depositional Environments of the Imo
1542 Shale Exposures at the Okigwe/Port Harcourt Express Road Junction Okigwe, Southeastern Nigeria,
1543 *Greener Journal of Physical Sciences*, 3, 255-272, ISSN: 2276-7851, 2013.

1544

1545 van Dijk, J., Fernandez, A., Bernasconi, S. M., Caves Rugenstein, J. K., Passey, S. R. and White, T.:
1546 Spatial pattern of super-greenhouse warmth controlled by elevated specific humidity, *Nat. Geosci.*,
1547 13, 739–744, <https://doi.org/10.1038/s41561-020-00648-2>, 2020.

1548

1549 Valdes, P. J., Armstrong, E., Badger, M. P. S., Bradshaw, C. D., Bragg, F., Crucifix, M., Davies-
1550 Barnard, T., Day, J. J., Farnsworth, A., Gordon, C., Hopcroft, P. O., Kennedy, A. T., Lord, N. S.,
1551 Lunt, D. J., Marzocchi, A., Parry, L. M., Pope, V., Roberts, W. H. G., Stone, E. J., Tourte, G. J. L. and
1552 Williams, J. H. T.: The BRIDGE HadCM3 family of climate models: HadCM3@Bristol v1.0, *Geosci.*
1553 *Model Dev.*, 10, 3715-3743, <https://doi.org/10.5194/gmd-10-3715-2017>, 2017.

1554

1555 Volodin, E. M. and Lykossov, V. N.: Parameterization of Heat and Moisture Transfer in the Soil-
1556 Vegetation System for Use in Atmospheric General Circulation Models: 2. Numerical Experiments in
1557 Climate Modeling, *Izvestiya Atmospheric and Oceanic Physics*, 34(5), 559-569, 1998.

1558

1559 Volodin, E. M., Mortikov, E. V., Kostykin, S. V., Galin, V. Y., Lykossov, V. N., Gritsun, A. S.,
1560 Diansky, N. A., Gusev, A. V. and Iakovlev, N. G.: Simulation of the present-day climate with the
1561 climate model INMCM5, *Clim. Dynam.*, 49, 3715-3734, [10.1007/s00382-017-3539-7](https://doi.org/10.1007/s00382-017-3539-7), 2017.

1562

1563 Volodin, E. M., Mortikov, E. V., Kostykin, S. V., Galin, V. Y., Lykossov, V. N., Gritsun, A. S.,
1564 Diansky, N. A., Gusev, A. V., Iakovlev, N. G., Shestakova, A. A. and Emelina, S. V.: Simulation of
1565 the modern climate using the INMCM48 climate model, *Russ. J. Numer. Anal. M.*, 33, 367-374,

1566 <https://doi.org/10.1515/rnam-2018-0032>, 2018.

1567

1568 West, C. K., Greenwood, D. R., Reichgelt, T., Lowe, A. J., Vachon, J. M., and Basinger, J. F.:
1569 Paleobotanical proxies for early Eocene climates and ecosystems in northern North America from
1570 middle to high latitudes, *Clim. Past*, 16, 1387-1410, <https://doi.org/10.5194/cp-16-1387-2020>, 2020.

1571

1572 Westerhold, T., Marwan, N., Drury, A. J., Liebrand, D., Agnini, C., Anagnostou, E., Barnet, J. S. K.,
1573 Bohaty, S. M., De Vleeschouwer, D., Florindo, F., Frederichs, T., Hodell, D. A., Holbourn, A. E.,
1574 Kroon, D., Laurentano, V., Littler, K., Lourens, L. J., Lyle, M., Pälike, H., Röhl, U., Tian, J., Wilkens,
1575 R. H., Wilson, P. A. and Zachos, J. C.: An astronomically dated record of Earth's climate and its
1576 predictability over the last 66 million years, *Science*, 369(6509), 1383-1387,
1577 <https://doi.org/10.1126/science.aba6853>, 2020.

1578

1579 Wilf, P., Wing, S. L., Greenwood, D. R. and Greenwood, C. L.: Using fossil leaves as
1580 paleoprecipitation indicators: An Eocene example, *Geology*, 26, 203-206,
1581 [https://doi.org/10.1130/0091-7613\(1998\)026<0203:UFLAPI>2.3.CO;2](https://doi.org/10.1130/0091-7613(1998)026<0203:UFLAPI>2.3.CO;2), 1998.

1582

1583 Williams, C. J. R.: Paleobotanical precipitation estimates used in Williams et al.: African
1584 hydroclimate monsoon during the early Eocene from the DeepMIP simulations, *Paleoceanography*
1585 and *Paleoclimatology*, 2022, (Version 1) [Dataset], Zenodo, DOI: 10.5281/zenodo.6472914, 2022.

1586

1587 Williams, C. J. R., Guarino, M.-V., Capron, E., Malmierca-Vallet, I., Singarayer, J. S., Sime, L. C.,
1588 Lunt, D. J. and Valdes, P. J.: CMIP6/PMIP4 simulations of the mid-Holocene and Last Interglacial
1589 using HadGEM3: comparison to the pre-industrial era, previous model versions and proxy data, *Clim.*
1590 *Past*, 16, 1429-1450, <https://doi.org/10.5194/cp-16-1429-2020>, 2020.

1591

1592 Williams, C. J. R. and Kniveton, D. R. (eds). *African Climate and Climate Change: Physical, Social*
1593 *and Political Perspectives*. Springer Science+Business Media BV 2011. Dordrecht, Heidelberg,
1594 London and New York: 212pp. DOI: 10.1007/978-90-481-3842-5, 2011.

1595

1596 Williams, C. J. R., Kniveton, D. R. and Layberry, R.: Climatic and oceanic associations with daily
1597 rainfall extremes over southern Africa, *Int. J. Clim.*, 27 (1): 93-108, <https://doi.org/10.1002/joc.1376>,
1598 2007.

1599

1600 Williams, C. J. R., Kniveton, D. R. and Layberry, R.: Influence of South Atlantic sea surface
1601 temperatures on rainfall variability and extremes over southern Africa, *J. Clim.*, 21: 6498-6520, DOI:
1602 <https://doi.org/10.1175/2008JCLI2234.1>, 2008.

1603
1604 Williams, C. J. R., Kniveton, D. R. and Layberry, R.: Assessment of a climate model to reproduce
1605 rainfall variability and extremes over southern Africa, *Theor. Applied Climatol.*, 99: 9-27, DOI:
1606 10.1007/s00704-009-0124-y, 2010.
1607
1608 Williams, C. J. R., Sellar, A. A., Ren, X., Haywood, A. M., Hopcroft, P., Hunter, S. J., Roberts, W. H.
1609 G., Smith, R. S., Stone, E. J., Tindall, J. C., and Lunt, D. J.: Simulation of the mid-Pliocene Warm
1610 Period using HadGEM3: experimental design and results from model–model and model–data
1611 comparison, *Clim. Past*, 17, 2139-2163, <https://doi.org/10.5194/cp-17-2139-2021>, 2021.
1612
1613 Willard, D. A., Donders, T. H., Reichgelt, T., Greenwood, D. R., Sangiorgi, F., Peterse, F., Nierop, K.
1614 G. J., Frieling, J., Schouten, S. and Sluijs, A.: Arctic vegetation, temperature, and hydrology during
1615 Early Eocene transient global warming events, *Global and Planetary Change*, 178, 139-152,
1616 <https://doi.org/10.1016/j.gloplacha.2019.04.012>, 2019.
1617
1618 Wright, I. J., Dong, N., Maire, V., Prentice, I. C., Westoby, M., Díaz, S., Gallagher, R. V., Jacobs, B.
1619 F., Kooyman, R., Law, E. A., Leishman, M. R., Niinemets, U., Reich, P. B., Sack, L., Villar, R.,
1620 Wang, H. and Wilf, P.: Global climatic drivers of leaf size, *Science*, 357(6354), 917–921, DOI:
1621 10.1126/science.aal4760, 2017.
1622
1623 Xie, Y. L., Wu, F. L. and Fang, X. M.: Middle Eocene East Asian monsoon prevalence over southern
1624 China: Evidence from palynological records, *Global and Planetary Change*, 175, 13-26, DOI:
1625 10.1016/j.gloplacha.2019.01.019, 2019.
1626
1627 Zhang, G. J. and McFarlane, N. A.: Sensitivity of climate simulations to the parameterization of
1628 cumulus convection in the Canadian Climate Centre general circulation model, *Atmosphere–Ocean*,
1629 33(3), 407-446, <https://doi.org/10.1080/07055900.1995.9649539>, 1995.
1630
1631 Zhang, M., Lin, W., Bretherton, C. S., Hack, J. J. and Rasch, P. J.: A modified formulation of
1632 fractional stratiform condensation rate in the NCAR Community Atmospheric Model (CAM2), *J.*
1633 *Geophys. Res.*, 108(D1), 4035, <https://doi.org/10.1029/2002JD002523>, 2003.
1634
1635 Zhu, J., Poulsen, C. J. and Otto-Bliesner, B. L.: High climate sensitivity in CMIP6 model not
1636 supported by paleoclimate, *Nat. Clim. Chang*, 10, 378-379, [https://doi.org/10.1038/s41558-020-0764-](https://doi.org/10.1038/s41558-020-0764-6)
1637 6, 2020.
1638
1639

